

# High-Fidelity Gradient-Based Wing Structural Optimization Including a Geometrically Nonlinear Flutter Constraint

Eirikur Jonsson <sup>\*</sup>, Cristina Riso <sup>†</sup>, Bernardo Bahia Monteiro <sup>‡</sup>, Alasdair C. Gray <sup>§</sup>,  
Joaquim R. R. A. Martins <sup>¶</sup>, and Carlos E. S. Cesnik <sup>||</sup>  
*University of Michigan, Ann Arbor, MI, 48109*

**Higher-aspect-ratio lightweight wings can make aircraft more energy efficient thanks to induced drag reduction. Because such wings exhibit large deflections, affecting the flutter onset, design optimization using linear flutter analysis is inadequate. To address this issue, we develop a framework for including a geometrically nonlinear flutter constraint into high-fidelity, gradient-based wing structural optimization. The framework evaluates the objective function (mass) and the stress and adjacency constraints in a built-up finite element model to capture the structural details of realistic wings. This built-up finite element model is reduced to a low-order beam representation to make geometrically nonlinear flutter analysis tractable for optimization. The geometrically nonlinear flutter analysis considers the wing deformed shape at each flight condition and aggregates the associated damping values into a scalar flutter constraint. The flutter constraint is differentiated with respect to the built-up structural sizing variables using the adjoint method to enable large-scale optimizations. The framework is demonstrated by minimizing the mass of a high-aspect-ratio wingbox subject to the geometrically nonlinear flutter constraint along with stress and adjacency constraints. The geometrically nonlinear flutter constraint introduces a mass penalty up to about 60% of the baseline mass compared with the 10% mass penalty by a linear flutter constraint based on the wing undeformed shape. This methodology can help design new-generation energy-efficient aircraft with high-aspect-ratio wings that require considering geometrically nonlinear effects early in the design cycle to prevent flutter.**

## I. Introduction

Climate change concerns are driving an interest in new aircraft designs with lightweight and high-aspect-ratio wings (HARWs) for higher energy efficiency [1]. While these aircraft can mitigate aviation environmental impacts, they pose new challenges to standard design practice based on linear aeroelasticity techniques [2]. These techniques are inapplicable to HARW aircraft because their high flexibility causes large aeroelastic deflections at normal operating conditions that invalid linear assumptions. Large aeroelastic deflections may cause flutter to occur at conditions that would be stable based on a linear flutter analysis of the wing undeformed shape [3–7]. This problem requires computing the flutter boundaries of HARW aircraft early in their design process, considering geometrically nonlinear effects.

A promising approach to consider flutter early in the design cycle of the next generation of HARW aircraft is to integrate a flutter constraint into design optimization [8]. This approach can produce energy-efficient aircraft designs requiring fewer late modifications by ensuring adequate flutter margins while minimizing mass or fuel burn. Despite the progress in including flutter constraints in practical aircraft design optimizations, only a few studies considered geometrically nonlinear effects [8]. Variyar et al. [9] minimized the fuel burn of a strut-braced aircraft subject to maneuver and gust constraints along with a geometrically nonlinear flutter speed constraint. They showed that the flutter constraint drives the design and causes a fuel burn penalty compared with considering only maneuver and gust constraints. Xie et al. [10] optimized the weight of a wind-tunnel wing model to ensure flutter in a given speed range and compared the results with and without considering static aeroelastic deflections in the flutter analysis. Lupp and Cesnik [11] minimized a blended wing-body aircraft fuel burn subject to a stress constraint and either a linear or a geometrically nonlinear flutter constraint.

<sup>\*</sup>Research Fellow, Department of Aerospace Engineering, 1320 Beal Avenue, AIAA Member, eirikurj@umich.edu

<sup>†</sup>Research Fellow, Department of Aerospace Engineering, 1320 Beal Avenue, AIAA Member, criso@umich.edu

<sup>‡</sup>Ph.D. Candidate, Department of Aerospace Engineering, 1320 Beal Avenue, AIAA Student Member, bbahia@umich.edu

<sup>§</sup>Ph.D. Candidate, Department of Aerospace Engineering, 1320 Beal Avenue, AIAA Student Member, alachris@umich.edu

<sup>¶</sup>Professor, Department of Aerospace Engineering, 1320 Beal Avenue, AIAA Fellow, jrram@umich.edu

<sup>||</sup>Clarence “Kelly” Johnson Professor, Department of Aerospace Engineering, 1320 Beal Avenue, AIAA Fellow, cesnik@umich.edu

The previous efforts evaluated the functions of interest (objective and constraints) using geometrically exact beam models; however, accurate stress analysis of realistic wings requires detailed structural modeling. To address this problem, this paper presents a framework for including a geometrically nonlinear flutter constraint into high-fidelity, gradient-based wing structural optimization. The framework evaluates the objective function (mass) and the stress and adjacency constraints in a built-up finite element model (FEM) that is reduced to a low-order beam representation for evaluating the flutter constraint. The flutter constraint is formulated as an aggregate of the damping values associated with a set of aeroelastic modes and operating conditions [12]. This formulation makes it possible to enforce this constraint using gradient-based optimization. The damping values at each operating condition are obtained from an aeroelastic eigenvalue analysis about the local wing deformed shape to capture geometrically nonlinear effects. The derivatives of the flutter constraint with respect to the built-up FEM structural sizing variables are obtained using the adjoint method to enable large-scale optimizations.

The paper is organized as follows: Sec. II presents the mathematical formulation of the geometrically nonlinear flutter constraint and its adjoint derivatives with respect to the built-up FEM structural sizing variables; Sec. III describes the computational framework that implements the proposed methodology; Sec. IV presents the wingbox test case; Sec. V discusses the optimization results obtained by minimizing the wingbox mass subject to the geometrically nonlinear flutter constraint at different root angles of attack, along with stress and adjacency constraints; and a section of concluding remarks ends the paper.

## II. Geometrically Nonlinear Flutter Constraint

This section describes the mathematical formulation of the geometrically nonlinear flutter constraint (Sec. II.A) and of its adjoint derivatives with respect to the built-up FEM structural sizing variables (Sec. II.B). Previous optimizations that included a geometrically nonlinear flutter constraint evaluated the objective and constraint functions in a beam model [9–11]. Here, the objective function (mass) and the stress and adjacency constraints are evaluated in a built-up FEM to capture realistic structural details; the flutter constraint is evaluated in a low-order beam representation derived from the built-up FEM to make geometrically nonlinear aeroelastic eigenvalue analyses tractable for optimization. This section describes the general methodology; Sec. III describes the computational implementation developed in this work.

### A. Function Evaluation

Figure 1 shows the process for evaluating the geometrically nonlinear flutter constraint within a high-fidelity, gradient-based wing structural optimization. The process considers  $N_d$  design variables listed in the vector  $\mathbf{x} \in \mathbb{R}^{N_d}$  representing shell element thicknesses—the inputs to the built-up FEM structural solver.

The built-up FEM at a given optimization step is reduced to a low-order beam representation for evaluating the geometrically nonlinear flutter constraint, with a computational effort tractable for optimization. The structural model reduction consists of computing equivalent inertia and stiffness distributions along a user-specified reference axis that is fixed in the optimization (Fig. 1). The equivalent inertia distributions consist of constitutive properties that relate the beam generalized forces to the corresponding generalized velocities; the equivalent stiffness distributions consist of constitutive properties that relate the beam generalized forces to the generalized strains.

The built-up FEM is discretized in  $N$  nodes with coordinates in the body frame listed in the vector  $\mathbf{p} \in \mathbb{R}^{3N}$ :

$$\mathbf{p} = \{p_{1_x}, \dots, p_{N_x}, p_{1_y}, \dots, p_{N_y}, p_{1_z}, \dots, p_{N_z}\}^T \quad (1)$$

The inertia distribution of the built-up FEM is described by its mass matrix  $\mathbf{M} = \mathbf{M}(\mathbf{x}) \in \mathbb{R}^{6N \times 6N}$  associated with the discretization nodes (e.g., MGG matrix in MSC Nastran). This matrix depends on the structural design variables  $\mathbf{x}$  and gives a set of nodal masses listed in the vector  $\mathbf{m} = \mathbf{m}(\mathbf{M}) \in \mathbb{R}^N$ :

$$\mathbf{m} = \{m_1, \dots, m_N\}^T \quad (2)$$

The nodal masses (2) are obtained by retaining one out of the three identical diagonal mass values for the translational degrees of freedom in the  $6 \times 6$  block of the mass matrix  $\mathbf{M}$  associated with each built-up FEM node. The mass matrix  $\mathbf{M}$  is often a diagonal matrix,  $\mathbf{M} = \mathbf{M}_D$ , that only provides three non-zero identical mass values per built-up FEM node. In some cases, this matrix is non diagonal and also provides offsets  $\delta \in \mathbb{R}^{3N}$  of the nodal masses  $\mathbf{m}$  with respect to the built-up FEM nodes  $\mathbf{p}$ :

$$\delta = \{\delta_{1_x}, \dots, \delta_{N_x}, \delta_{1_y}, \dots, \delta_{N_y}, \delta_{1_z}, \dots, \delta_{N_z}\}^T \quad (3)$$

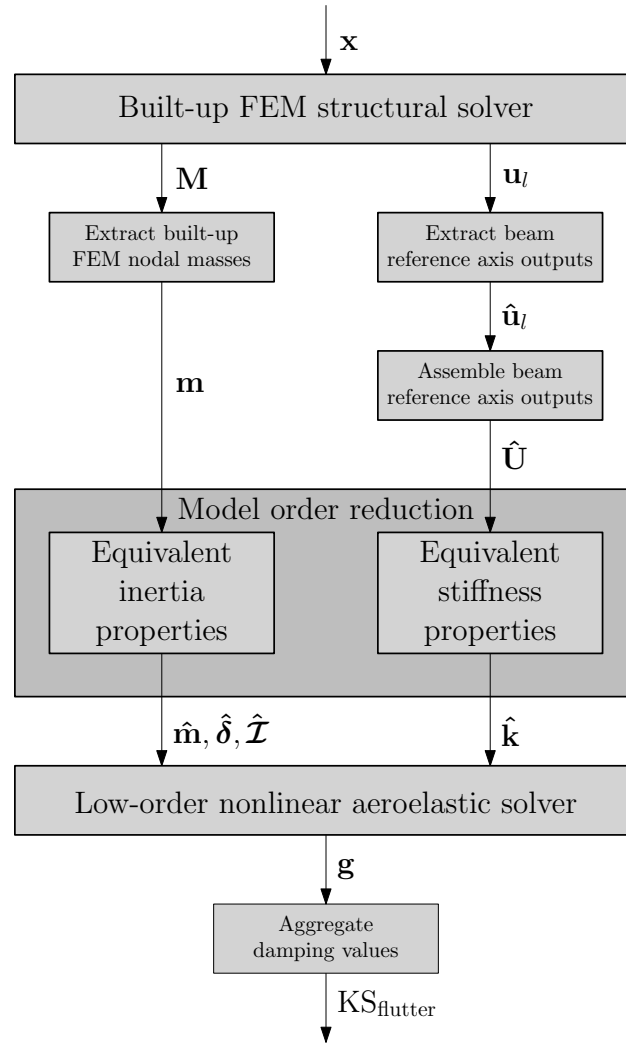


**Fig. 1 Geometrically nonlinear flutter constraint evaluation process.**

Futhermore, the built-up FEM mass matrix can also provide inertia tensors  $\mathcal{I} \in \mathbb{R}^{6N}$  about the points  $\mathbf{p} + \delta$ :

$$\mathcal{I} = \{\mathcal{I}_{1xx}, \dots, \mathcal{I}_{Nxx}, \mathcal{I}_{1yy}, \dots, \mathcal{I}_{Nyy}, \mathcal{I}_{1zz}, \dots, \mathcal{I}_{Nzz}, \mathcal{I}_{1xy}, \dots, \mathcal{I}_{Nxy}, \mathcal{I}_{1xz}, \dots, \mathcal{I}_{Nxz}, \mathcal{I}_{1yz}, \dots, \mathcal{I}_{Nyz}\}^T \quad (4)$$

The mass offsets (3) and inertia tensors (4) are non zero when the built-up FEM contains beam or shell elements having offsets with respect to the built-up FEM nodes or rigid-body elements (e.g., MSC Nastran CONM2 elements) with offsets and concentrated inertias.

The equivalent inertia distributions of the built-up FEM are given by a set of masses  $\hat{\mathbf{m}} \in \mathbb{R}^{\hat{N}}$ , mass offsets  $\hat{\delta} \in \mathbb{R}^{3\hat{N}}$ , and inertia tensors  $\hat{\mathcal{I}} \in \mathbb{R}^{6\hat{N}}$  associated with  $\hat{N}$  nodes along a user-specified beam reference axis. The masses  $\hat{\mathbf{m}}$  are listed in the vector

$$\hat{\mathbf{m}} = \{\hat{m}_1, \dots, \hat{m}_{\hat{N}}\}^T \quad (5)$$

and are associated with the beam reference axis nodes of body-frame coordinates listed in the vector  $\hat{\mathbf{p}} \in \mathbb{R}^{3\hat{N}}$ :

$$\hat{\mathbf{p}} = \{\hat{p}_{1x}, \dots, \hat{p}_{\hat{N}x}, \hat{p}_{1y}, \dots, \hat{p}_{\hat{N}y}, \hat{p}_{1z}, \dots, \hat{p}_{\hat{N}z}\}^T \quad (6)$$

The masses  $\hat{\mathbf{m}}$  may also have offsets  $\hat{\delta} \in \mathbb{R}^{3\hat{N}}$  with respect to the points  $\hat{\mathbf{p}}$ :

$$\hat{\delta} = \{\hat{\delta}_{1x}, \dots, \hat{\delta}_{\hat{N}x}, \hat{\delta}_{1y}, \dots, \hat{\delta}_{\hat{N}y}, \hat{\delta}_{1z}, \dots, \hat{\delta}_{\hat{N}z}\}^T \quad (7)$$

along with inertia tensors  $\hat{\mathcal{I}} \in \mathbb{R}^{6\hat{N}}$  about the points  $\hat{\mathbf{p}} + \hat{\delta}$ :

$$\hat{\mathcal{I}} = \{\hat{\mathcal{I}}_{1xx}, \dots, \hat{\mathcal{I}}_{\hat{N}xx}, \hat{\mathcal{I}}_{1yy}, \dots, \hat{\mathcal{I}}_{\hat{N}yy}, \hat{\mathcal{I}}_{1zz}, \dots, \hat{\mathcal{I}}_{\hat{N}zz}, \hat{\mathcal{I}}_{1xy}, \dots, \hat{\mathcal{I}}_{\hat{N}xy}, \hat{\mathcal{I}}_{1xz}, \dots, \hat{\mathcal{I}}_{\hat{N}xz}, \hat{\mathcal{I}}_{1yz}, \dots, \hat{\mathcal{I}}_{\hat{N}yz}\}^T \quad (8)$$

The masses  $\hat{\mathbf{m}}$ , mass offsets  $\hat{\delta}$ , and inertia tensors  $\hat{\mathcal{I}}$  in Eqs. (5), (7), and (8) depend on the built-up FEM mass matrix through the nodal masses  $\mathbf{m}$  in Eq. (2), that is,  $\hat{\mathbf{m}}, \hat{\delta}, \hat{\mathcal{I}} = \hat{\mathbf{m}}(\mathbf{m}), \hat{\delta}(\mathbf{m}), \hat{\mathcal{I}}(\mathbf{m})$ . In a general case, these quantities also depend on the mass offsets and inertia tensors provided by the built-up FEM mass matrix, given in Eqs. (3) and (4). This dependency is omitted here because the mass offsets and inertia tensors associated with the built-up FEM nodes are assumed to be only due to rigid-body elements representing non-structural mass distributions that remain fixed during the optimization. The quantities  $\hat{\mathbf{m}}, \hat{\delta}, \hat{\mathcal{I}}$  in Eqs. (5), (7), and (8) provide the equivalent inertia distributions of the built-up FEM for the geometrically nonlinear flutter analysis.

The equivalent stiffness distributions of the built-up FEM are computed via a structural identification process based on a set of linear static solutions. These distributions are described by the vector  $\hat{\mathbf{k}} \in \mathbb{R}^{10\hat{M}}$ , where  $\hat{M} = \hat{N} - 1$  is the number of elements defined by pairs of consecutive beam reference axis nodes:

$$\hat{\mathbf{k}} = \{\hat{\mathbf{k}}_{11}^T, \hat{\mathbf{k}}_{22}^T, \hat{\mathbf{k}}_{33}^T, \hat{\mathbf{k}}_{44}^T, \hat{\mathbf{k}}_{12}^T, \hat{\mathbf{k}}_{13}^T, \hat{\mathbf{k}}_{14}^T, \hat{\mathbf{k}}_{23}^T, \hat{\mathbf{k}}_{24}^T, \hat{\mathbf{k}}_{34}^T\}^T \quad (9)$$

$$\begin{aligned} \hat{\mathbf{k}}_{11} &= \{\hat{k}_{111}, \dots, \hat{k}_{\hat{M}_{11}}\}^T & \hat{\mathbf{k}}_{22} &= \{\hat{k}_{122}, \dots, \hat{k}_{\hat{M}_{22}}\}^T & \hat{\mathbf{k}}_{33} &= \{\hat{k}_{133}, \dots, \hat{k}_{\hat{M}_{33}}\}^T \\ \hat{\mathbf{k}}_{44} &= \{\hat{k}_{144}, \dots, \hat{k}_{\hat{M}_{44}}\}^T & \hat{\mathbf{k}}_{12} &= \{\hat{k}_{112}, \dots, \hat{k}_{\hat{M}_{12}}\}^T & \hat{\mathbf{k}}_{13} &= \{\hat{k}_{113}, \dots, \hat{k}_{\hat{M}_{13}}\}^T \\ \hat{\mathbf{k}}_{14} &= \{\hat{k}_{114}, \dots, \hat{k}_{\hat{M}_{14}}\}^T & \hat{\mathbf{k}}_{23} &= \{\hat{k}_{123}, \dots, \hat{k}_{\hat{M}_{23}}\}^T & \hat{\mathbf{k}}_{24} &= \{\hat{k}_{124}, \dots, \hat{k}_{\hat{M}_{24}}\}^T \\ \hat{\mathbf{k}}_{34} &= \{\hat{k}_{134}, \dots, \hat{k}_{\hat{M}_{34}}\}^T \end{aligned} \quad (10)$$

In this work, the quantities in Eqs. (9) and (10) describe the  $4 \times 4$  cross-sectional stiffness matrix constants associated with each beam element according to the strain-based geometrically exact beam formulation of Su and Cesnik [13]. These quantities are a function of the assembled displacement outputs (translations and rotations) of the beam reference axis nodes resulting from six independent static load cases applied to the built-up FEM,  $\hat{\mathbf{k}} = \hat{\mathbf{k}}(\hat{\mathbf{U}})$ .

The assembled displacement output vector  $\hat{\mathbf{U}} \in \mathbb{R}^{36\hat{N}}$  is obtained as follows. The built-up FEM displacement vector for a generic load case,  $\mathbf{u} = \mathbf{u}(\mathbf{x}) \in \mathbb{R}^{6N}$ , depends implicitly on the design variables  $\mathbf{x}$  through the solution of a linear static structural analysis. The displacement vector for the  $l$ th load case used for stiffness identification is denoted by  $\mathbf{u}_l$ , that is,  $\mathbf{u}_1 \dots \mathbf{u}_l \dots \mathbf{u}_6$  are the displacement vectors for the six independent load cases—typically, three tip forces and three tip moments. The stiffness identification does not require the displacement output vector of the entire built-up FEM but only the one of the beam reference axis nodes, which is recovered via interpolation elements (e.g., MSC Nastran RBE3 elements). The displacement outputs at the beam reference axis nodes are extracted from the

full displacement output  $\mathbf{u}_l$  for the  $l$ th load case using a search process and are stacked into  $\hat{\mathbf{u}}_l$ . This process is written as  $\hat{\mathbf{u}}_l = \hat{\mathbf{u}}_l(\mathbf{u}_l) \in \mathbb{R}^{6\hat{N}}$  and gives

$$\hat{\mathbf{u}}_l = \{\hat{u}_{l,11}, \dots, \hat{u}_{l,16}, \dots, \hat{u}_{l,j1}, \dots, \hat{u}_{l,j6}, \dots, \hat{u}_{l,\hat{N}1}, \dots, \hat{u}_{l,\hat{N}6}\}^T \quad (11)$$

where  $\hat{u}_{l,j1}$  is the displacement output for the first degree of freedom of the  $j$ th beam reference axis node for the  $l$ th load case. The linear static displacements of the beam reference axis nodes for the six independent load cases are assembled into the output vector

$$\hat{\mathbf{U}} = \hat{\mathbf{U}}(\hat{\mathbf{u}}_1, \hat{\mathbf{u}}_2, \hat{\mathbf{u}}_3, \hat{\mathbf{u}}_4, \hat{\mathbf{u}}_5, \hat{\mathbf{u}}_6) \quad (12)$$

This vector is built by extracting the  $k$ th displacement output for the  $j$ th reference axis node and  $l$ th load case, given by  $\hat{u}_{l,jk}$ , such that

$$\begin{aligned} \hat{\mathbf{U}} = \{ & \hat{u}_{1,11}, \dots, \hat{u}_{1,16}, \dots, \hat{u}_{1,11}, \dots, \hat{u}_{1,16}, \dots, \hat{u}_{6,11}, \dots, \hat{u}_{6,16}, \\ & \hat{u}_{1,21}, \dots, \hat{u}_{1,26}, \dots, \hat{u}_{1,21}, \dots, \hat{u}_{1,26}, \dots, \hat{u}_{6,21}, \dots, \hat{u}_{6,26}, \\ & \dots, \\ & \hat{u}_{1,j1}, \dots, \hat{u}_{1,j6}, \dots, \hat{u}_{1,j1}, \dots, \hat{u}_{1,j6}, \dots, \hat{u}_{6,j1}, \dots, \hat{u}_{6,j6}, \\ & \dots, \\ & \hat{u}_{1,\hat{N}1}, \dots, \hat{u}_{1,\hat{N}6}, \dots, \hat{u}_{1,\hat{N}1}, \dots, \hat{u}_{1,\hat{N}6}, \dots, \hat{u}_{6,\hat{N}1}, \dots, \hat{u}_{6,\hat{N}6} \}^T \end{aligned} \quad (13)$$

The assembled displacement vector in Eq. (13) is used to compute the equivalent beam stiffness distributions of the built-up FEM using the methodology detailed in Refs. [14, 15].

The equivalent inertia and stiffness distributions associated with the user-specified beam reference axis define the low-order beam representation of the built-up FEM at a given optimization step. In this work, the low-order beam representation is coupled to the potential-flow unsteady airfoil theory of Peters’ et al. [16] to obtain the aeroelastic model for evaluating the geometrically nonlinear flutter constraint.

The geometrically nonlinear flutter constraint builds on the damping-based formulation proposed in Ref. [12] and its geometrically nonlinear extension [11]. Consider a nonlinear aeroelastic system governed by

$$\dot{\mathbf{y}} = \mathbf{f}(\mathbf{y}(\mathbf{c}, \mathbf{x}), \mathbf{c}, \mathbf{x}) \quad (14)$$

The quantity  $\mathbf{y}$  in Eq. (14) is the  $N_y \times 1$  state vector and  $\mathbf{c}$  is the  $N_c \times 1$  vector of control parameters. These control parameters identify a point in the flight envelope in terms of boundary conditions (*e.g.*, load factor or angle of attack) and flight conditions (*e.g.*, Mach number and altitude).

The stability of the nonlinear aeroelastic system (14) for a fixed design  $\mathbf{x}$  is assessed by choosing  $N_s$  flight envelope points  $\mathbf{c}_i$  of interest for the stability analysis ( $i = 1, \dots, N_s$ ). Each flight envelope point  $\mathbf{c}_i$  is associated with an equilibrium state  $\mathbf{y}_{e_i}(\mathbf{x}) := \mathbf{y}_e(\mathbf{c}_i, \mathbf{x})$  that satisfies

$$\mathbf{f}(\mathbf{y}_{e_i}(\mathbf{x}), \mathbf{c}_i, \mathbf{x}) = \mathbf{0} \quad (15)$$

The small-amplitude dynamics about the equilibrium state  $\mathbf{y}_{e_i}(\mathbf{x})$  is governed by the linearized equation

$$\Delta \dot{\mathbf{y}} = \mathbf{A}_i(\mathbf{x}) \Delta \mathbf{y} \quad (16)$$

where  $\Delta \mathbf{y} := \mathbf{y} - \mathbf{y}_{e_i}$  is the  $N \times 1$  state perturbation vector and

$$\mathbf{A}_i(\mathbf{x}) := \left. \frac{\partial \mathbf{f}(\mathbf{y}(\mathbf{c}, \mathbf{x}), \mathbf{c}, \mathbf{x})}{\partial \mathbf{y}} \right|_{\mathbf{y}(\mathbf{c}, \mathbf{x}) = \mathbf{y}_{e_i}(\mathbf{x}), \mathbf{c} = \mathbf{c}_i} \quad (17)$$

is the  $N_y \times N_y$  Jacobian matrix of the system (14) with respect to the state vector  $\mathbf{y}$  evaluated at the equilibrium state  $\mathbf{y}_{e_i}$ . The eigenvalues of  $\mathbf{A}_i(\mathbf{x})$  are denoted by  $\sigma_{ik}(\mathbf{x}) := g_{ik}(\mathbf{x}) + j\omega_{ik}(\mathbf{x})$  ( $k = 1, \dots, N_y$ ), where  $g_{ik}(\mathbf{x})$  is the damping associated with the  $k$ th mode at the  $i$ th equilibrium state,  $\omega_{ik}(\mathbf{x})$  the corresponding angular frequency, and  $j$  the imaginary unit.

The equilibrium state  $\mathbf{y}_{e_i}(\mathbf{x})$  associated with the  $i$ th flight envelope point  $\mathbf{c}_i$  is stable if the damping values  $g_{ik}(\mathbf{x})$  are all negative. This requirement translates to the set of damping-based flutter constraints

$$g'_{ik}(\mathbf{x}) := g_{ik}(\mathbf{x}) - G_i \leq 0 \quad \begin{aligned} & \forall i = 1, \dots, N_s \\ & \forall k = 1, \dots, N_m \end{aligned} \quad (18)$$

where  $N_m \leq N_y$  is the number of modes considered for enforcing the flutter constraint, which may be lower than the total number of modes associated with Eq. (16). The quantity  $G_i = G(\mathbf{c}_i)$  in Eq. (18) is the value of a damping bounding curve at the flight envelope point  $\mathbf{c}_i$  that increases the design robustness by allowing for a residual damping when the flutter constraint is active [12].

The constraints (18) are suitable for gradient-based optimization because they are continuous, smooth, and differentiable functions of the design variables [8]. Because their large number  $N_s \times N_m$  makes computing derivatives unfeasible in practical problems, Eq. (18) is reduced to a scalar constraint using the Kreisselmeier-Steinhauser (KS) aggregation function [17–19]. The aggregation enables computing derivatives efficiently using adjoint methods that scale with the number of outputs but are independent of the number of design variables.

Assuming a constraint value of the aggregation parameter  $\rho_{KS}$  for all the modes and equilibrium states gives

$$\text{KS}_{\text{flutter}}(\mathbf{x}) := g'_{\max}(\mathbf{x}) + \frac{1}{\rho_{KS}} \ln \left\{ \sum_{i=1}^{N_s} \sum_{k=1}^{N_m} \exp \{ \rho_{KS} [g'_{ik}(\mathbf{x}) - g'_{\max}(\mathbf{x})] \} \right\} \leq 0 \quad (19)$$

This scalar flutter constraint is a conservative estimate of the most positive bounded damping value in Eq. (18), denoted by  $g'_{\max}(\mathbf{x})$ , and tends to that quantity as the aggregation parameter tends to infinity [19].

## B. Adjoint Derivatives

The geometrically nonlinear flutter constraint dependency on the structural design variables associated with the built-up FEM sizing can be represented as

$$\text{KS}_{\text{flutter}}(\mathbf{x}) = \text{KS}(\mathbf{g}') \quad (20)$$

$$= \text{KS}(\mathbf{g}'(\hat{\mathbf{k}}, \hat{\mathbf{m}}, \hat{\delta}, \hat{\mathcal{I}})) \quad (21)$$

$$= \text{KS}(\mathbf{g}'(\hat{\mathbf{k}}(\hat{\mathbf{U}}), \hat{\mathbf{m}}(\mathbf{m}), \hat{\delta}(\mathbf{m}), \hat{\mathcal{I}}(\mathbf{m}))) \quad (22)$$

$$= \text{KS}(\mathbf{g}'(\hat{\mathbf{k}}(\hat{\mathbf{U}}), \hat{\mathbf{m}}(\mathbf{m}(\mathbf{M})), \hat{\delta}(\mathbf{m}(\mathbf{M})), \hat{\mathcal{I}}(\mathbf{m}(\mathbf{M})))) \quad (23)$$

$$= \text{KS}(\mathbf{g}'(\hat{\mathbf{k}}(\hat{\mathbf{U}}(\hat{\mathbf{u}}_1, \dots, \hat{\mathbf{u}}_6)), \hat{\mathbf{m}}(\mathbf{m}(\mathbf{M})), \hat{\delta}(\mathbf{m}(\mathbf{M})), \hat{\mathcal{I}}(\mathbf{m}(\mathbf{M})))) \quad (24)$$

$$= \text{KS}(\mathbf{g}'(\hat{\mathbf{k}}(\hat{\mathbf{U}}(\hat{\mathbf{u}}_1(\mathbf{u}_1(\mathbf{x})), \dots, \hat{\mathbf{u}}_6(\mathbf{u}_6(\mathbf{x})))), \hat{\mathbf{m}}(\mathbf{m}(\mathbf{M}(\mathbf{x}))), \hat{\delta}(\mathbf{m}(\mathbf{M}(\mathbf{x}))), \hat{\mathcal{I}}(\mathbf{m}(\mathbf{M}(\mathbf{x})))))) \quad (25)$$

This functional dependency yields the adjoint derivative formulation developed below.

### 1. Derivative Definitions

The functions of interest are listed in the  $N_f \times 1$  vector  $\mathcal{F}$ . For a given set of control parameters  $\mathbf{c} = \mathbf{c}_i$ , these functions depend on the design variables  $\mathbf{x}$  and on the state variables of the system  $\mathbf{y}(\mathbf{x})$ , which depend implicitly on the design variables:

$$\mathcal{F} = \mathcal{F}(\mathbf{x}, \mathbf{y}(\mathbf{x})) \quad (26)$$

where the residual equation is

$$\mathbf{R} = \mathbf{R}(\mathbf{x}, \mathbf{y}(\mathbf{x})) = \mathbf{0} \quad (27)$$

The total derivative of the functions of interest is

$$\frac{d\mathcal{F}}{d\mathbf{x}} = \frac{\partial \mathcal{F}}{\partial \mathbf{x}} + \frac{\partial \mathcal{F}}{\partial \mathbf{y}} \frac{d\mathbf{y}}{d\mathbf{x}} \quad (28)$$

and the total derivative of the residual equation is

$$\frac{d\mathbf{R}}{d\mathbf{x}} = \frac{\partial \mathbf{R}}{\partial \mathbf{x}} + \frac{\partial \mathbf{R}}{\partial \mathbf{y}} \frac{d\mathbf{y}}{d\mathbf{x}} = \mathbf{0} \quad (29)$$

Rearranging Eq. (29) gives

$$\frac{\partial \mathbf{R}}{\partial \mathbf{y}} \frac{d\mathbf{y}}{d\mathbf{x}} = - \frac{\partial \mathbf{R}}{\partial \mathbf{x}} \quad (30)$$

$$\frac{d\mathbf{y}}{d\mathbf{x}} = - \left[ \frac{\partial \mathbf{R}}{\partial \mathbf{y}} \right]^{-1} \frac{\partial \mathbf{R}}{\partial \mathbf{x}} \quad (31)$$

and combining this relation with Eq. (28) gives

$$\frac{d\mathcal{F}}{d\mathbf{x}} = \frac{\partial\mathcal{F}}{\partial\mathbf{x}} - \frac{\partial\mathcal{F}}{\partial\mathbf{y}} \left[ \frac{\partial\mathbf{R}}{\partial\mathbf{y}} \right]^{-1} \frac{\partial\mathbf{R}}{\partial\mathbf{x}} \quad (32)$$

This total derivative can be computed using the *direct* or *adjoint* method. The *adjoint* equations are written as

$$\left[ \frac{\partial\mathbf{R}}{\partial\mathbf{y}} \right]^T \boldsymbol{\psi} = \left[ \frac{\partial\mathcal{F}}{\partial\mathbf{y}} \right]^T \quad (33)$$

where  $\boldsymbol{\psi}$  is the  $N_d \times N_f$  adjoint matrix. The  $i$ th column is the adjoint vector  $\boldsymbol{\psi}_i$  from a linear solve with a right-hand side of  $[\partial\mathcal{F}_i/\partial\mathbf{y}]^T$  for the  $i$ th function of interest. Computing the adjoint matrix requires  $N_f$  linear solves. Next, substituting into Eq. (32) gives

$$\frac{d\mathcal{F}}{d\mathbf{x}} = \frac{\partial\mathcal{F}}{\partial\mathbf{x}} - \boldsymbol{\psi}^T \frac{\partial\mathbf{R}}{\partial\mathbf{x}} \quad (34)$$

Alternatively, one can use the *direct* method

$$\frac{\partial\mathbf{R}}{\partial\mathbf{y}} \frac{d\mathbf{y}}{d\mathbf{x}} = \frac{\partial\mathbf{R}}{\partial\mathbf{x}} \quad (35)$$

$$\frac{\partial\mathbf{R}}{\partial\mathbf{y}} \boldsymbol{\phi} = \frac{\partial\mathbf{R}}{\partial\mathbf{x}} \quad (36)$$

This linear system needs to be solved  $N_d$  times to get the full  $d\mathbf{y}/d\mathbf{x}$ . The  $i$ th column is the direct vector  $\boldsymbol{\phi}_i$  from a linear solve with a right-hand side of  $[\partial\mathbf{R}/\partial x_i]$  for the  $i$ th design variable. Once the entire matrix  $\boldsymbol{\phi}$  is known, one obtains

$$\frac{d\mathcal{F}}{d\mathbf{x}} = \frac{\partial\mathcal{F}}{\partial\mathbf{x}} - \frac{\partial\mathbf{R}}{\partial\mathbf{x}} \boldsymbol{\phi} \quad (37)$$

In this work, the total derivatives are computed using the adjoint method to enable large-scale optimizations with many design variables but few outputs of interest (objective and constraint functions). The adjoint method is the most suitable for these problems because it does not scale with the number of design variables. The derivation below assumes that the derivatives associated with all blocks in Fig. 1 are known and the derivative  $\partial\mathbf{KS}_{\text{flutter}}/\partial\mathbf{u}_l$  for the  $l$ th load case exists. One can use the adjoint equation (33) by substituting the  $l$ th derivative in for the right-hand side and by solving the linear system:

$$\left[ \frac{\partial\mathbf{R}_l}{\partial\mathbf{u}_l} \right]^T \boldsymbol{\psi}_l = \left[ \frac{\partial\mathbf{KS}_{\text{flutter}}}{\partial\mathbf{u}_l} \right]^T \quad (38)$$

This linear system needs to be solved for six load cases associated with the linear static solutions used in the equivalent stiffness identification. Next, the total derivative of the flutter constraint with respect to the build-up FEM structural sizing variables is

$$\frac{d\mathbf{KS}_{\text{flutter}}}{d\mathbf{x}} = \frac{\partial\mathbf{KS}_{\text{flutter}}}{\partial\mathbf{x}} - \sum_{l=1}^6 \left( \boldsymbol{\psi}_l^T \frac{\partial\mathbf{R}_l}{\partial\mathbf{x}} \right) \quad (39)$$

The derivation of each term necessary for computing Eq. (38) and (39) is reported below.

## 2. Computing $\partial\mathbf{KS}_{\text{flutter}}/\partial\mathbf{x}$

To compute  $\partial\mathbf{KS}_{\text{flutter}}/\partial\mathbf{x}$ , one needs to vary the design variables while keeping the state variables (displacement outputs of the linear static solutions) fixed and re-evaluate the aggregated constraint. The partial derivative chain is given by

$$\frac{\partial\mathbf{KS}_{\text{flutter}}}{\partial\mathbf{x}} = \frac{\partial\mathbf{KS}_{\text{flutter}}}{\partial\mathbf{g}} \frac{\partial\mathbf{g}}{\partial\hat{\mathbf{k}}} \frac{\partial\hat{\mathbf{k}}}{\partial\hat{\mathbf{U}}} \frac{\partial\hat{\mathbf{U}}}{\partial\mathbf{x}} + \frac{\partial\mathbf{KS}_{\text{flutter}}}{\partial\mathbf{g}} \left( \frac{\partial\mathbf{g}}{\partial\hat{\mathbf{m}}} \frac{\partial\hat{\mathbf{m}}}{\partial\mathbf{m}} + \frac{\partial\mathbf{g}}{\partial\hat{\delta}} \frac{\partial\hat{\delta}}{\partial\mathbf{m}} + \frac{\partial\mathbf{g}}{\partial\hat{\mathcal{I}}} \frac{\partial\hat{\mathcal{I}}}{\partial\mathbf{m}} \right) \frac{\partial\mathbf{m}}{\partial\mathbf{M}_D} \frac{\partial\mathbf{M}_D}{\partial\mathbf{x}} \quad (40)$$

$$= \frac{\partial\mathbf{KS}_{\text{flutter}}}{\partial\mathbf{g}} \left[ \frac{\partial\mathbf{g}}{\partial\hat{\mathbf{k}}} \frac{\partial\hat{\mathbf{k}}}{\partial\hat{\mathbf{U}}} \frac{\partial\hat{\mathbf{U}}}{\partial\mathbf{x}} + \left( \frac{\partial\mathbf{g}}{\partial\hat{\mathbf{m}}} \frac{\partial\hat{\mathbf{m}}}{\partial\mathbf{m}} + \frac{\partial\mathbf{g}}{\partial\hat{\delta}} \frac{\partial\hat{\delta}}{\partial\mathbf{m}} + \frac{\partial\mathbf{g}}{\partial\hat{\mathcal{I}}} \frac{\partial\hat{\mathcal{I}}}{\partial\mathbf{m}} \right) \frac{\partial\mathbf{m}}{\partial\mathbf{M}_D} \frac{\partial\mathbf{M}_D}{\partial\mathbf{x}} \right] \quad (41)$$

$$= \frac{\partial\mathbf{KS}_{\text{flutter}}}{\partial\mathbf{g}} \left( \frac{\partial\mathbf{g}}{\partial\hat{\mathbf{m}}} \frac{\partial\hat{\mathbf{m}}}{\partial\mathbf{m}} + \frac{\partial\mathbf{g}}{\partial\hat{\delta}} \frac{\partial\hat{\delta}}{\partial\mathbf{m}} + \frac{\partial\mathbf{g}}{\partial\hat{\mathcal{I}}} \frac{\partial\hat{\mathcal{I}}}{\partial\mathbf{m}} \right) \frac{\partial\mathbf{m}}{\partial\mathbf{M}_D} \frac{\partial\mathbf{M}_D}{\partial\mathbf{x}} \quad (42)$$



This calculation uses  $\partial \mathbf{M}/\partial \mathbf{x} = \partial \mathbf{M}_D/\partial \mathbf{x}$  that holds because the quantities  $\delta$  and  $\mathcal{I}$  do not play a role in Eq. (40) as they are associated with rigid-body elements that are not optimized.

Additionally, differentiating and expanding  $\partial \hat{\mathbf{U}}/\partial \mathbf{x}$  one has

$$\frac{\partial \hat{\mathbf{U}}}{\partial \mathbf{x}} = \frac{\partial \hat{\mathbf{U}}}{\partial \hat{\mathbf{u}}_1} \frac{\partial \hat{\mathbf{u}}_1}{\partial \mathbf{u}_1} \frac{\partial \mathbf{u}_1}{\partial \mathbf{x}} + \frac{\partial \hat{\mathbf{U}}}{\partial \hat{\mathbf{u}}_2} \frac{\partial \hat{\mathbf{u}}_2}{\partial \mathbf{u}_2} \frac{\partial \mathbf{u}_2}{\partial \mathbf{x}} + \dots + \frac{\partial \hat{\mathbf{U}}}{\partial \hat{\mathbf{u}}_6} \frac{\partial \hat{\mathbf{u}}_6}{\partial \mathbf{u}_6} \frac{\partial \mathbf{u}_6}{\partial \mathbf{x}} \quad (43)$$

$$= \sum_{l=1}^6 \left( \frac{\partial \hat{\mathbf{U}}}{\partial \hat{\mathbf{u}}_l} \frac{\partial \hat{\mathbf{u}}_l}{\partial \mathbf{u}_l} \frac{\partial \mathbf{u}_l}{\partial \mathbf{x}} \right) = \mathbf{0} \quad (44)$$

This term is zero because the states (displacement outputs from the linear static solution) depend implicitly but not explicitly on the design variables,  $\partial \mathbf{u}_l/\partial \mathbf{x} = \mathbf{0}$ .

By differentiating Eq. (25) with respect to the displacement outputs for the  $l$ th static load case,  $\mathbf{u}_l$ , the partial derivative can be written as

$$\frac{\partial \text{KS}_{\text{flutter}}}{\partial \mathbf{u}_l} = \frac{\partial \text{KS}_{\text{flutter}}}{\partial \mathbf{g}} \left[ \frac{\partial \mathbf{g}}{\partial \hat{\mathbf{k}}} \frac{\partial \hat{\mathbf{k}}}{\partial \hat{\mathbf{U}}} \frac{\partial \hat{\mathbf{U}}}{\partial \mathbf{u}_l} + \frac{\partial \mathbf{g}}{\partial \hat{\mathbf{m}}} \frac{\partial \hat{\mathbf{m}}}{\partial \hat{\mathbf{U}}} \frac{\partial \hat{\mathbf{U}}}{\partial \mathbf{u}_l} + \frac{\partial \mathbf{g}}{\partial \hat{\delta}} \frac{\partial \hat{\delta}}{\partial \hat{\mathbf{U}}} \frac{\partial \hat{\mathbf{U}}}{\partial \mathbf{u}_l} + \frac{\partial \mathbf{g}}{\partial \hat{\mathcal{I}}} \frac{\partial \hat{\mathcal{I}}}{\partial \hat{\mathbf{U}}} \frac{\partial \hat{\mathbf{U}}}{\partial \mathbf{u}_l} \right] \quad (45)$$

$$= \frac{\partial \text{KS}_{\text{flutter}}}{\partial \mathbf{g}} \frac{\partial \mathbf{g}}{\partial \hat{\mathbf{k}}} \frac{\partial \hat{\mathbf{k}}}{\partial \hat{\mathbf{U}}} \frac{\partial \hat{\mathbf{U}}}{\partial \mathbf{u}_l} \quad (46)$$

The terms  $\partial \hat{\mathbf{m}}/\partial \hat{\mathbf{U}} = \partial \hat{\delta}/\partial \hat{\mathbf{U}} = \partial \hat{\mathcal{I}}/\partial \hat{\mathbf{U}} = \mathbf{0}$  because the equivalent inertia distributions are independent of the displacement outputs needed to identify the equivalent stiffness distributions. Rewriting as transpose for adjoint equation of efficient matrix-vector products gives

$$\frac{\partial \text{KS}_{\text{flutter}}}{\partial \mathbf{u}_l}^T = \frac{\partial \hat{\mathbf{u}}_l^T}{\partial \mathbf{u}_l} \frac{\partial \hat{\mathbf{U}}^T}{\partial \hat{\mathbf{u}}_l} \frac{\partial \hat{\mathbf{k}}^T}{\partial \hat{\mathbf{U}}} \frac{\partial \mathbf{g}^T}{\partial \hat{\mathbf{k}}} \frac{\partial \text{KS}_{\text{flutter}}}{\partial \mathbf{g}}^T \quad (47)$$

The different partial derivatives involved in the above relations from the KS aggregation, low-order flutter analysis, and structural model order reduction, and built-up FEM static solutions are grouped as follows:

$$\underbrace{\frac{\partial \text{KS}_{\text{flutter}}}{\partial \mathbf{g}}}_{\text{KS aggregation}} \underbrace{\frac{\partial \mathbf{g}}{\partial \hat{\mathbf{k}}}, \frac{\partial \mathbf{g}}{\partial \hat{\mathbf{m}}}, \frac{\partial \mathbf{g}}{\partial \hat{\delta}}, \frac{\partial \mathbf{g}}{\partial \hat{\mathcal{I}}}}_{\text{Low-order flutter analysis}} \underbrace{\frac{\partial \hat{\mathbf{k}}}{\partial \hat{\mathbf{U}}}, \frac{\partial \hat{\mathbf{m}}}{\partial \mathbf{m}}, \frac{\partial \hat{\delta}}{\partial \mathbf{m}}, \frac{\partial \hat{\mathcal{I}}}{\partial \mathbf{m}}}_{\text{Model order reduction}} \underbrace{\frac{\partial \mathbf{m}}{\partial \mathbf{M}_D}, \frac{\partial \hat{\mathbf{U}}}{\partial \hat{\mathbf{u}}_l}, \frac{\partial \hat{\mathbf{u}}_l}{\partial \mathbf{u}_l}}_{\text{Pre-processing}} \underbrace{\frac{\partial \mathbf{u}_l}{\partial \mathbf{x}} = \mathbf{0}, \frac{\partial \mathbf{M}_D}{\partial \mathbf{x}}}_{\text{Built-up FEM}} \quad (48)$$

The calculation of these terms is discussed below.

### 3. Computing $\partial \mathbf{m}/\partial \mathbf{M}_D$ and $\partial \mathbf{M}_D/\partial \mathbf{x}$

The derivatives of the built-up FEM mass matrix  $\partial \mathbf{M}_D/\partial \mathbf{x}$  are provided by built-up FEM structural solver and are not detailed here, see Ref. [20] for details about the implementation used in this work. The operation  $\mathbf{m} \rightarrow \mathbf{M}_D$  is a reduction operation, thus the derivative  $\partial \mathbf{m}/\partial \mathbf{M}_D$  is a sparse matrix of zeros and ones.

### 4. Computing $\partial \hat{\mathbf{U}}/\partial \hat{\mathbf{u}}_l$ and $\partial \hat{\mathbf{u}}_l/\partial \mathbf{u}_l$

Extracting the displacement vectors  $\hat{\mathbf{u}}_l$  associated with the beam reference axis nodes from the built-up FEM displacement vectors  $\mathbf{u}_l$  and the assembly operations for stacking these elements into the vector  $\mathbf{U}$  are a mapping and a permutation operation, respectively, whose derivatives are given by sparse matrices of ones and zeros. For instance,  $\partial \hat{\mathbf{U}}/\partial \hat{\mathbf{u}}_l$  is a permutation operation, resulting in a partially filled identity matrix that serves to select only the derivatives related to  $\hat{\mathbf{u}}_l$ .

### 5. Computing Equivalent Inertia Distribution Derivatives

The equivalent inertia distributions are differentiated analytically to compute the partial derivatives  $\partial \hat{\mathbf{m}}/\partial \mathbf{m}$ ,  $\partial \hat{\delta}/\partial \mathbf{m}$ , and  $\partial \hat{\mathcal{I}}/\partial \mathbf{m}$ . For optimizations including only structural designs variables considered in this work, these derivatives are computed for a fixed discretization of the built-up FEM and of the beam reference axis.



The mass  $\hat{m}_j$  of the rigid-body element at the  $j$ th beam reference axis node ( $j = 1, \dots, \hat{N}$ ) is the sum of the nodal masses of the  $N_j$  built-up FEM nodes its nearest neighbor:

$$\hat{m}_j = \sum_{i=1}^{N_j} m_i \quad (49)$$

The derivative of Eq. (49) with respect to the mass  $m_k$  associated with the  $k$ th built-up FEM node in the nearest neighbor of the  $j$ th beam reference axis node is

$$\frac{\partial \hat{m}_j}{\partial m_k} = \sum_{i=1}^{N_j} \frac{\partial m_i}{\partial m_k} = 1 \quad (50)$$

If the  $k$ th built-up FEM node does not belong to the nearest neighbor of the  $j$ th beam reference axis node, its nodal mass does not play a role in Eq. (49) and the derivative (50) is zero. Because Eq. (49) does not depend on the other built-up FEM mass matrix data, the associated derivatives are also zero:

$$\begin{aligned} \frac{\partial \hat{m}_j}{\partial \delta_{k_x}} &= 0 & \frac{\partial \hat{m}_j}{\partial \delta_{k_y}} &= 0 & \frac{\partial \hat{m}_j}{\partial \delta_{k_z}} &= 0 \\ \frac{\partial \hat{m}_j}{\partial \mathcal{I}_{k_{xx}}} &= 0 & \frac{\partial \hat{m}_j}{\partial \mathcal{I}_{k_{yy}}} &= 0 & \frac{\partial \hat{m}_j}{\partial \mathcal{I}_{k_{zz}}} &= 0 \\ \frac{\partial \hat{m}_j}{\partial \mathcal{I}_{k_{xy}}} &= 0 & \frac{\partial \hat{m}_j}{\partial \mathcal{I}_{k_{xz}}} &= 0 & \frac{\partial \hat{m}_j}{\partial \mathcal{I}_{k_{yz}}} &= 0 \end{aligned} \quad (51)$$

The mass offset components  $\hat{\delta}_{j_x}$ ,  $\hat{\delta}_{j_y}$ , and  $\hat{\delta}_{j_z}$  of the rigid-body element at the  $j$ th beam reference axis node are

$$\begin{aligned} \hat{\delta}_{j_x} &= \frac{1}{\hat{m}_j} \sum_{i=1}^{N_j} m_i (p_{i_x} + \delta_{i_x} - \hat{p}_{j_x}) \\ \hat{\delta}_{j_y} &= \frac{1}{\hat{m}_j} \sum_{i=1}^{N_j} m_i (p_{i_y} + \delta_{i_y} - \hat{p}_{j_y}) \\ \hat{\delta}_{j_z} &= \frac{1}{\hat{m}_j} \sum_{i=1}^{N_j} m_i (p_{i_z} + \delta_{i_z} - \hat{p}_{j_z}) \end{aligned} \quad (52)$$

The derivatives of Eq. (52) with respect to the built-up FEM mass matrix data are reported for  $\hat{\delta}_{j_x}$  only because the derivatives for the other mass offset components in Eq. (52) are given by similar relations.

The derivative of  $\hat{\delta}_{j_x}$  with respect to the mass  $m_k$  associated with the  $k$ th built-up FEM node in the nearest neighbor of the  $j$ th beam reference axis node is given by

$$\frac{\partial \hat{\delta}_{j_x}}{\partial m_k} = \frac{1}{\hat{m}_j} [(p_{k_x} + \delta_{k_x}) - (\hat{p}_{j_x} + \hat{\delta}_{j_x})] \quad (53)$$

The derivatives with respect to the mass offset components associated with the  $k$ th built-up FEM node are

$$\frac{\partial \hat{\delta}_{j_x}}{\partial \delta_{k_x}} = \frac{m_k}{\hat{m}_j} \quad \frac{\partial \hat{\delta}_{j_y}}{\partial \delta_{k_y}} = 0 \quad \frac{\partial \hat{\delta}_{j_z}}{\partial \delta_{k_z}} = 0 \quad (54)$$

If the  $k$ th built-up FEM node does not belong to the nearest neighbor of the  $j$ th beam reference axis node, the derivatives (53) and (54) are zero. Because Eq. (49) does not depend on the built-up FEM inertia tensor data, the associated derivatives are also zero:

$$\frac{\partial \hat{\delta}_{j_x}}{\partial \mathcal{I}_{k_{xx}}} = 0 \quad \frac{\partial \hat{\delta}_{j_x}}{\partial \mathcal{I}_{k_{yy}}} = 0 \quad \frac{\partial \hat{\delta}_{j_x}}{\partial \mathcal{I}_{k_{zz}}} = 0 \quad \frac{\partial \hat{\delta}_{j_x}}{\partial \mathcal{I}_{k_{xy}}} = 0 \quad \frac{\partial \hat{\delta}_{j_x}}{\partial \mathcal{I}_{k_{xz}}} = 0 \quad \frac{\partial \hat{\delta}_{j_x}}{\partial \mathcal{I}_{k_{yz}}} = 0 \quad (55)$$

The independent components of the inertia tensor of the rigid-body element at the  $j$ th beam reference axis node ( $j = 1, \dots, N_j$ ) about the local center of mass are given by

$$\begin{aligned}
 \hat{I}_{jxx} &= \sum_{i=1}^{N_j} I_{ixx} + \sum_{i=1}^{N_j} m_i \{[(p_{iy} + \delta_{iy}) - (p_{jy} + \hat{\delta}_{iy})]^2 + [(p_{iz} + \delta_{iz}) - (\hat{p}_{jz} + \hat{\delta}_{jz})]^2\} \\
 \hat{I}_{jyy} &= \sum_{i=1}^{N_j} I_{iyy} + \sum_{i=1}^{N_j} m_i \{[(p_{ix} + \delta_{ix}) - (p_{jx} + \hat{\delta}_{jx})]^2 + [(p_{iz} + \delta_{iz}) - (\hat{p}_{jz} + \hat{\delta}_{jz})]^2\} \\
 \hat{I}_{jzz} &= \sum_{i=1}^{N_j} I_{izz} + \sum_{i=1}^{N_j} m_i \{[(p_{ix} + \delta_{ix}) - (p_{jx} + \hat{\delta}_{jx})]^2 + [(p_{iy} + \delta_{iy}) - (\hat{p}_{jy} + \hat{\delta}_{jy})]^2\} \\
 \hat{I}_{jxy} &= \sum_{i=1}^{N_j} I_{ixy} - \sum_{i=1}^{N_j} m_i [(p_{ix} + \delta_{ix}) - (p_{jx} + \hat{\delta}_{jx})][(p_{iy} + \delta_{iy}) - (\hat{p}_{jy} + \hat{\delta}_{jy})] \\
 \hat{I}_{jxz} &= \sum_{i=1}^{N_j} I_{ixz} - \sum_{i=1}^{N_j} m_i [(p_{ix} + \delta_{ix}) - (p_{jx} + \hat{\delta}_{jx})][(p_{iz} + \delta_{iz}) - (\hat{p}_{jz} + \hat{\delta}_{jz})] \\
 \hat{I}_{jyz} &= \sum_{i=1}^{N_j} I_{iyz} - \sum_{i=1}^{N_j} m_i [(p_{iy} + \delta_{iy}) - (p_{jy} + \hat{\delta}_{jy})][(p_{iz} + \delta_{iz}) - (\hat{p}_{jz} + \hat{\delta}_{jz})]
 \end{aligned} \tag{56}$$

The derivatives of Eq. (56) with respect to the built-up FEM lumped mass matrix data are reported for the  $\hat{I}_{jxx}$  and  $\hat{I}_{jxy}$  components because the derivatives for the other components in Eq. (56) are given by similar relations.

The derivatives of  $\hat{I}_{jxx}$  with respect to the mass  $m_k$  associated with the  $k$ th built-up FEM node in the nearest neighbor of the  $j$ th beam reference axis node is given by

$$\frac{\partial \hat{I}_{jxx}}{\partial m_k} = [(p_{ky} + \delta_{ky}) - (\hat{p}_{jy} + \hat{\delta}_{jy})]^2 + [(p_{kz} + \delta_{kz}) - (\hat{p}_{jz} + \hat{\delta}_{jz})]^2 \tag{57}$$

The derivatives with respect to the mass offset components associated with the  $k$ th built-up FEM node are

$$\frac{\partial \hat{I}_{jxx}}{\partial \delta_{kx}} = 0 \quad \frac{\partial \hat{I}_{jxx}}{\partial \delta_{ky}} = 2 m_k [(p_{ky} + \delta_{ky}) - (\hat{p}_{jy} + \hat{\delta}_{jy})] \quad \frac{\partial \hat{I}_{jxx}}{\partial \delta_{kz}} = 2 m_k [(p_{kz} + \delta_{kz}) - (\hat{p}_{jz} + \hat{\delta}_{jz})] \tag{58}$$

The derivatives with respect to the inertia tensor components for the  $k$ th built-up FEM node are

$$\frac{\partial \hat{I}_{jxx}}{\partial I_{kxx}} = 1 \quad \frac{\partial \hat{I}_{jxx}}{\partial I_{kyy}} = 0 \quad \frac{\partial \hat{I}_{jxx}}{\partial I_{kzz}} = 0 \quad \frac{\partial \hat{I}_{jxx}}{\partial I_{kxy}} = 0 \quad \frac{\partial \hat{I}_{jxx}}{\partial I_{kxz}} = 0 \quad \frac{\partial \hat{I}_{jxx}}{\partial I_{kyz}} = 0 \tag{59}$$

If the  $k$ th built-up FEM node does not belong to the nearest neighbor of the  $j$ th beam reference axis node, the derivatives (57) to (59) are all zero.

For the off-diagonal component  $\hat{I}_{jxy}$ , Eq. (57) becomes

$$\frac{\partial \hat{I}_{jxy}}{\partial m_k} = -[(p_{kx} + \delta_{kx}) - (\hat{p}_{jx} + \hat{\delta}_{jx})][(p_{ky} + \delta_{ky}) - (\hat{p}_{jy} + \hat{\delta}_{jy})] \tag{60}$$

Equation (58) becomes

$$\frac{\partial \hat{I}_{jxy}}{\partial \delta_{kx}} = -m_k [(p_{ky} + \delta_{ky}) - (\hat{p}_{jy} + \hat{\delta}_{jy})] \quad \frac{\partial \hat{I}_{jxy}}{\partial \delta_{ky}} = -m_k [(p_{kx} + \delta_{kx}) - (\hat{p}_{jx} + \hat{\delta}_{jx})] \quad \frac{\partial \hat{I}_{jxy}}{\partial \delta_{kz}} = 0 \tag{61}$$

Finally:

$$\frac{\partial \hat{I}_{jxy}}{\partial I_{kxx}} = 0 \quad \frac{\partial \hat{I}_{jxy}}{\partial I_{kyy}} = 0 \quad \frac{\partial \hat{I}_{jxy}}{\partial I_{kzz}} = 0 \quad \frac{\partial \hat{I}_{jxy}}{\partial I_{kxy}} = 1 \quad \frac{\partial \hat{I}_{jxy}}{\partial I_{kxz}} = 0 \quad \frac{\partial \hat{I}_{jxy}}{\partial I_{kyz}} = 0 \tag{62}$$

If the  $k$ th built-up FEM node is not in the nearest neighbor of the  $j$ th beam reference axis node, the derivatives (60) to (62) are zero.

The analytical derivatives in this section are simplified using the definition of local center of mass associated with the  $k$  beam reference axis node:

$$\begin{aligned}\frac{1}{\hat{m}_j} \sum_{i=1}^{N_j} m_i [(p_{i_x} + \delta_{i_x}) - (\hat{p}_{j_x} + \hat{\delta}_{j_x})] &= 0 \\ \frac{1}{\hat{m}_j} \sum_{i=1}^{N_j} m_i [(p_{i_y} + \delta_{i_y}) - (\hat{p}_{j_y} + \hat{\delta}_{j_y})] &= 0 \\ \frac{1}{\hat{m}_j} \sum_{i=1}^{N_j} m_i [(p_{i_z} + \delta_{i_z}) - (\hat{p}_{j_z} + \hat{\delta}_{j_z})] &= 0\end{aligned}\tag{63}$$

The derivatives with respect to the built-up FEM mass offsets and inertia tensors are reported for completeness, but not used in this work where these quantities are associated with rigid-body elements representing non-structural mass distributions that are not optimized.

### 6. Computing Equivalent Stiffness Distribution Derivatives

The equivalent stiffness distributions in Fig. (1) are differentiated numerically using the complex-step method to compute the partial derivatives  $\partial \hat{\mathbf{k}} / \partial \hat{\mathbf{U}}$ . A finite-difference implementation is developed for verification.

Figure 2 shows a high-level schematic of the equivalent stiffness identification (see Refs. [14, 15] for details on each block). The stiffness module inputs are the  $3N \times 1$  vector  $\mathbf{p}$  listing the built-up FEM node coordinates, the  $3\hat{N} \times 1$  vector  $\hat{\mathbf{p}}$  listing the coordinates of the beam reference axis nodes, and the  $36\hat{N} \times 1$  vector  $\hat{\mathbf{U}}$  of the built-up FEM static displacements (translations and rotations) for the six static load cases at the beam reference axis nodes. The module output is the  $10(\hat{N} - 1) \times 1$  vector  $\hat{\mathbf{k}}$  of the equivalent stiffness distributions describing the low-order beam representation of the built-up FEM based on the formulation of Su and Cesnik [13]. Because the quantities  $\mathbf{p}$  and  $\hat{\mathbf{p}}$  are constant in optimizations that consider only structural sizing variables, the equivalent stiffness module is differentiated to compute only the partials  $\partial \hat{\mathbf{k}} / \partial \hat{\mathbf{U}}$ .

### 7. Computing Flutter Analysis and Aggregation Derivatives

The flutter analysis and constraint aggregation are differentiated in part analytically and in part using automated differentiation (AD) to compute the partial derivatives  $\partial \mathbf{g} / \partial \hat{\mathbf{k}}$ ,  $\partial \mathbf{g} / \partial \hat{\mathbf{m}}$ ,  $\partial \mathbf{g} / \partial \hat{\delta}$  and  $\partial \mathbf{g} / \partial \hat{\mathbf{T}}$  and  $\partial \text{KS}_{\text{flutter}} / \partial \mathbf{g}$ .

The flutter analysis involves linearizing the equations of motion about the equilibrium states at selected flight conditions to obtain the state-space matrices in Eq. (16) and extract their eigenvalues. The real part of the eigenvalues (damping) are bounded by a safety margin and aggregated to evaluate the flutter constraint in Eq. (19). The aggregation is conducted in two steps by first aggregating all the bounded damping values for different modes at each flight condition and by then aggregating the resulting quantities over the flight conditions.

The linearization process leverages a nonlinear aeroelastic framework described in Sec. III, the University of Michigan’s Nonlinear Aeroelastic Simulation Toolbox (UM/NAST) [6]. In this work, a AD-based module associated with UM/NAST was developed to compute the derivatives of the nested KS aggregation (over the modes for a given flight condition) to obtain the partial derivatives of the aggregate values with respect to the equivalent beam inertia and stiffness distributions. The derivatives of the outer KS aggregation are given by the analytical derivatives of the KS function, and the two sets of derivatives are coupled to compute the derivatives of the flutter constraint with respect to the equivalent inertia and stiffness distributions. A finite-difference calculation is also developed for verifying the AD implementation.

## III. Computational Implementation

This section describes the computational framework for high-fidelity, gradient-based wing structural optimization that implements the methodology of Sec. II. The novel contribution from this work consists of coupling the modules described below to evaluate the geometrically nonlinear flutter constraint, obtaining the partial derivatives of each module, and evaluating the constraint adjoint derivatives with respect to the built-up FEM structural sizing variables.

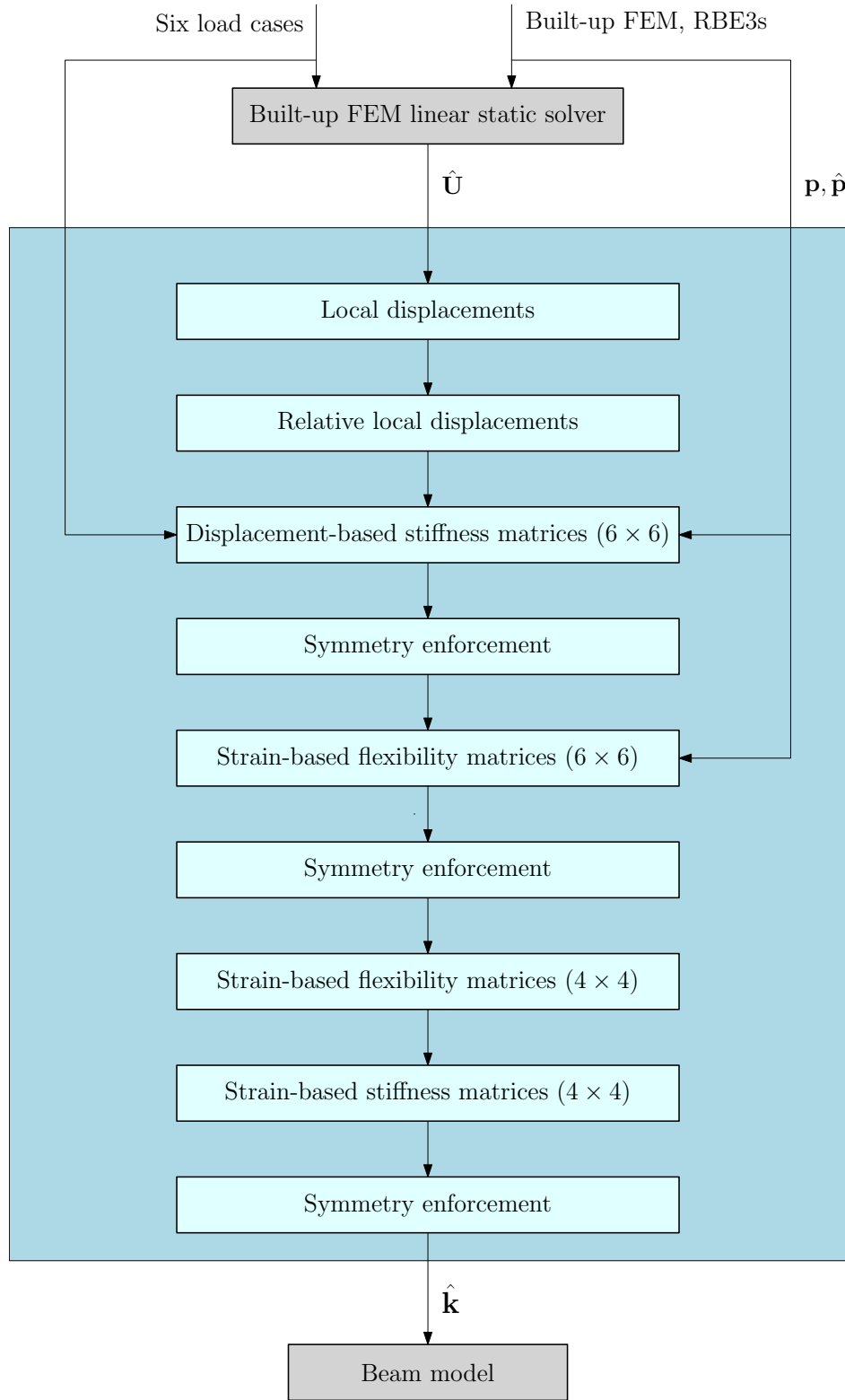


**Fig. 2** Computational procedure for equivalent stiffness module.

### A. Optimization Algorithm

The optimization algorithm is SNOPT (Sparse Nonlinear OPTimizer) [21], a gradient-based optimizer that implements a sequential quadratic programming (SQP) algorithm. SNOPT uses an augmented Lagrangian merit function; the Hessian of the Lagrangian is approximated using a quasi-Newton approach that is suited to optimization problems with many sparse nonlinear constraints. The interface with SNOPT is handled by pyOptSparse\* [22], an implementation of pyOpt [23] that eases defining large sparse Jacobians crucial to the performance of large scale optimizers like SNOPT.

### B. High-Fidelity Structural Analysis

The structural analysis solver is the Toolkit for the Analysis of Composite Structures (TACS) [20].<sup>†</sup>, an open-source parallel finite element solver that handles poorly conditioned problems common in aircraft thin-walled structures. For such cases, the stiffness matrix condition numbers may exceed  $O(10^9)$ , but TACS can solve these poorly conditioned problems using a Schur-complement-based parallel direct solver. Sensitivities of structural functions of interest with respect to structural and geometric design variables are computed efficiently using the adjoint method [20].

### C. Low-Order Flutter Analysis

The geometrically nonlinear flutter constraint is evaluated based on damping values from aeroelastic eigenvalue analyses about the equilibrium states at selected flight conditions. These eigenvalue analyses are conducted in UM/NAST [6], a low-order multidisciplinary framework for modeling, analyzing, and simulating very flexible wings and complete aircraft in free flight.

UM/NAST describes an aircraft as a set of beams representing different components (wing, fuselage, etc.) that undergo arbitrary structural deflections relative to a body-fixed frame in rigid-body motion within an inertial frame. Structural deflections are described by the strain-based, geometrically exact beam formulation of Su and Cesnik [13], which uses element strains (axial extension and bending/torsion curvatures) as the independent degrees of freedom and recovers the deformed shape by integrating nonlinear kinematic relations [6, 13].

UM/NAST handles different loads including gravity, point/distributed forces and moments, and aerodynamics. Aerodynamic loads can be computed using multiple formulations, such as the potential-flow unsteady airfoil theory of Peters et al. [16] used in this work. This formulation assumes strip theory: the aerodynamic loads at the cross sections of the beam element nodes depend only on the local flow and control parameters (angle of attack, Mach number, etc.). These aerodynamic loads may be corrected for compressibility, sweep, or tip losses using analytical relations. Unsteady aerodynamic effects are captured by a set of aerodynamic states representing inflow expansions [16].

This work leverages the UM/NAST capability to conduct aeroelastic eigenvalue analyses in the frequency domain. The process consist of linearizing the nonlinear equations of motion about the equilibrium states at chosen flight envelope points to compute the local state-space matrices, extract their eigenvalues, and post-processing them to compute the flutter point. The post-processing is skipped for optimization because the flutter constraint is posed on the damping values rather the flutter point.

### D. Structural Model Order Reduction

To evaluate the geometrically nonlinear flutter constraint it requires reducing the built-up FEM in TACS at a given optimization step to an equivalent beam representation in UM/NAST (see Sec. II). The equivalent beam distributions of the TACS built-up FEM are computed using the University of Michigan’s Enhanced FEM2Stick (UM/EF2S) code [14, 15], which has been enhanced with derivative capabilities. The outputs from EF2S are fed to UM/NAST to compute the geometrically nonlinear flutter constraint and its derivatives with respect to the equivalent inertia and stiffness distributions. The total derivatives of the geometrically nonlinear flutter constraint with respect to the built-up FEM structural design variables used in TACS are obtained from the adjoint formulation introduced in Sec. II.B.

## IV. Optimization Problem

This section describes the optimization problem used for demonstrating the proposed methodology. Section IV.A describes the baseline wingbox being optimized and Sec. IV.B reports the optimization problem statement.

---

\*<https://github.com/mdolab/pyoptsparse>

<sup>†</sup><https://github.com/gjkennedy/tacs>

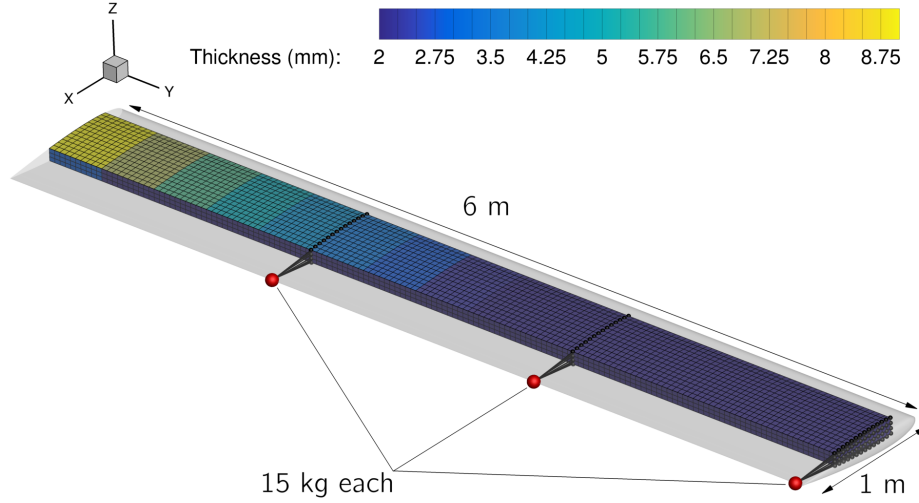


**Fig. 3 Baseline wing model.**

### A. Baseline Model

The baseline wing model is shown in Fig. 3. The model consists of a rectangular, untwisted wing with a unit chord, an aspect ratio of 12, and a constant NACA 0012 aerodynamic cross section. The structural wingbox spans from 15% to 65% of the aerodynamic chord and its sizing is determined from a preliminary structural optimization under representative 2.5 g aerodynamic loads, without a flutter constraint. The resulting optimized structural mass is 68.5 kg. The wingbox model is completed by three 15-kg non-structural point masses along the trailing edge at each third of the semispan. These non-structural masses make the baseline model flutter over a range of flight speeds and angles of attack that result in a sensible range of static aeroelastic deformed shapes. Because the non-structural masses are not optimized, they are included into the UM/NAST equivalent beam model of the wingbox as rigid-body elements that are not differentiated against, differently from the structural equivalent inertia distributions that are updated at each step.

To evaluate the geometrically nonlinear flutter constraint, the wingbox built-up FEM in TACS is condensed to an equivalent beam model in UM/NAST at each optimization step. The beam reference axis is at 41% of the aerodynamic chord and is discretized in 8 reference nodes corresponding to 7 three-node beam finite elements in UM/NAST. For the stiffness condensation, each beam reference axis node is connected to the leading and trailing edges of its corresponding cross section by an interpolation element akin to a MSC Nastran RBE3 element. Figure 4 shows the TACS and UM/NAST models overlapped. The equivalent beam model in UM/NAST is coupled to a potential-flow unsteady thin airfoil model [16] with a zero-thickness, flat-plate cross section. The resulting low-order aeroelastic model is used for evaluating the geometrically nonlinear flutter constraint while the other functions of interest are evaluated on the built-up FEM directly. This choice allows for capturing realistic structural details and their influence on the wing mass and stress levels while keeping the geometrically nonlinear flutter analysis tractable for the optimization.

### B. Optimization Statement

Table 1 summarizes the optimization problem for demonstrating the methodology of Sec. II. The optimization minimizes the wingbox mass by varying the thickness of the skin, spar, and rib panels. Each wingbox panel is treated as a non-stiffened shell element and given its own thickness variable, resulting in 76 structural sizing variables.

The primary constraint is the geometrically nonlinear flutter constraint evaluated in UM/NAST based on the formulation of Section II.A. This constraint aggregates the damping values from a set of aeroelastic eigenvalue analyses at fixed angle of attack and varying speed. The aggregation provides a continuous, smooth, and differentiable approximation to the most positive damping value for a given design. The damping values are bounded by a threshold of 0.12 rad/s that is constant with speed and are aggregated using a constant aggregation parameter  $\rho_{KS} = 100$  for all modes and flight conditions. The positive threshold is introduced to avoid constraint violations associated with marginally stable in-plane modes, achieving a similar effect as adding structural damping.

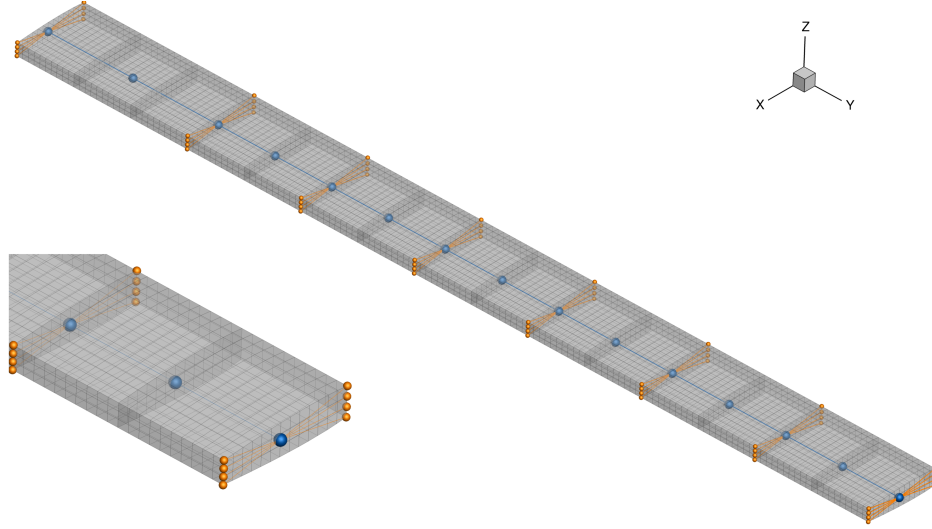


**Fig. 4** Baseline wing TACS and UM/NAST structural models.

**Table 1** Optimization formulation.

|                 | Function/variable  | Description                                | Quantity |
|-----------------|--|--|----------|
| minimize        | $M$  | Wingbox mass                               |          |
| with respect to | $t$  | Panel thicknesses of skins/spars/ribs      | 76       |
| subject to      | $KS_{\text{flutter}} \leq 0$                             | KS aggregate of modal damping values       | 1        |
|                 | $KS_{\text{stress}} \leq 1$                              | KS aggregates of 2.5 g Yield stress values | 4        |
|                 | $ t_{\text{skin}, i} - t_{\text{skin}, i+1}  \leq 0.005$ | Skin adjacency constraints                 | 28       |
|                 | $ t_{\text{spar}, i} - t_{\text{spar}, i+1}  \leq 0.005$ | Spar adjacency constraints                 | 28       |

In addition to the geometrically nonlinear flutter constraint, the optimization includes stress constraints. Each panel is constrained not to exceed its failure criterion at a representative 2.5 g flight condition. The constraints for groups of panels are KS-aggregated to reduce the total number of constraints, resulting in four failure constraints: one for the upper skins, one for the lower skins, one for both spars, and one for the ribs. The stress constraints are evaluated in the built-up FEM subject to pre-computed loads to allow for a more accurate representation of the wingbox stress levels. The optimization also includes a set of linear adjacency constraints that limit the thickness change between any two adjacent skin or spar panels to be less than 5 mm. These constraints enforce more realistic structural designs and improve the optimizer performance by limiting the design space, even in cases where the adjacency constraints are not active.

Three optimization problems are solved by evaluating the geometrically nonlinear flutter constraint for different values of the root angle of attack  $\alpha = 0^\circ, 3^\circ$ , and  $6^\circ$ . These cases are considered to investigate the impact of geometrically nonlinear effects on the optimal design. For zero angle of attack, the geometrically nonlinear flutter constraint reduces to a linear flutter constraint that considers the wing undeformed shape; for non-zero angle of attack, the wing experiences static aeroelastic deflections (which vary with the flight condition) that modify the flutter boundary and the constraint value, leading to different results. The flutter analysis considers the speed range  $V = 10 \rightarrow 180$  m/s sampled with 10 equally spaced points and assumes sea-level conditions. These conditions, subject to the specified angles of attack, are chosen to result in no, medium, and large static aeroelastic displacements. Subsonic compressibility effects are handled by means of the Prandtl-Glauert correction and unsteady aerodynamic effects by adding six inflow states per beam element according to the potential-flow unsteady thin airfoil theory of Peters et al. [16]. Three-dimensional aerodynamic effects are not considered in the flutter analysis, but they will be incorporated as a future development. This could be done by applying a tip loss factor correction to the strip theory model, or by specifying a variable lift curve slope along the span derived from a three-dimensional aerodynamic model (e.g., CFD model).



**Table 2** Verification of the total derivatives of the flutter constraint  $KS_{\text{flutter}}$  with respect to selected structural design variables (relative finite-difference step size  $h = 10^{-3}$ ).

| Design variable            | Derivative formulation |             | $\Delta$ (%)            |
|----------------------------|------------------------|-------------|-------------------------|
|                            | Finite difference      | Adjoint     |                         |
| $x_{\text{Rib 4}}$         | −14.108794             | −14.114520  | $4.0586 \times 10^{-2}$ |
| $x_{\text{Front spar 4}}$  | −739.824090            | −739.809480 | $1.9747 \times 10^{-3}$ |
| $x_{\text{Rear spar 4}}$   | −615.554519            | −615.548978 | $9.0021 \times 10^{-4}$ |
| $x_{\text{Upper skin 12}}$ | −900.766347            | −900.753299 | $1.4486 \times 10^{-3}$ |
| $x_{\text{Lower skin 12}}$ | −900.415733            | −900.398323 | $1.9335 \times 10^{-3}$ |

### C. Derivative verification

The total derivatives of the geometrically nonlinear flutter constraint with respect to the built-up FEM structural sizing variables are verified by comparing the values computed from the developed adjoint formulation (Sec. II.B) with a second-order central finite-difference approximation applied to the entire derivative chain:

$$\frac{d\mathcal{F}}{d\mathbf{x}} = \frac{\mathcal{F}(\mathbf{x} + h) - \mathcal{F}(\mathbf{x} - h)}{2h} + O(h^2).$$

A step-size study is performed, and the resulting relative step used for the verification is  $h = 10^{-3}$ . Table 2 compares the derivatives for selected design variables computed using the finite-difference approximation and the adjoint formulation. The derivative values agree with each other for all design variables, showing relative errors from about 0.001% to 0.04%. The level of agreement for the total derivatives reported in Table 2 is representative of all the total derivatives: the average relative difference between the finite-difference and adjoint results is 0.005%.

## V. Optimization Results

Table 3 summarizes the objective function value and state of the constraints of the optimized designs. The wingbox mass (objective function) is impacted by including the flutter constraint. For the  $\alpha = 0^\circ$  case, resulting in a linear flutter analysis of the wing undeformed shape, the mass penalty due to the flutter constraint is 11.1% of the baseline mass. In the non-zero angle of attack cases  $\alpha = 3^\circ$  and  $6^\circ$ , the wing experiences static aeroelastic deflections, which vary with speed, resulting in a geometrically nonlinear flutter analysis. In these cases, the mass penalty increases to 38.1% and 52.7% of the baseline mass—more than three and five times the mass penalty from the linear flutter constraint—demonstrating the importance of considering geometrically nonlinear effects when optimizing high-aspect-ratio wings.

The stress constraints on the ribs and spars are inactive for all optimized designs, while the stress constraints on the upper skins are always active. The stress constraints on the lower skins are active for the baseline and the  $\alpha = 0^\circ$  case but are not active for the  $\alpha = 3^\circ$  and  $\alpha = 6^\circ$  cases. This behavior can be explained by analyzing the structural sizing for each optimized design along with its difference compared to the baseline, shown in Fig. 5. The optimized designs increase the thickness of the spars, upper, and lower skins, with higher angle of attack to satisfy the added flutter constraint. The increased thickness of the spars results in smaller deflections, which mitigates the skin stress levels. Thickness also increases substantially for the lower skins in the  $\alpha = 3^\circ$  and  $\alpha = 6^\circ$  cases compared with the baseline and the  $\alpha = 0^\circ$ , more than for the upper skins.

A detailed mass breakdown for each group of components is given in Table 4. Except for the optimized design at  $\alpha = 0^\circ$ , all ribs remain unchanged, at the lower bound, compared with the baseline wing. All optimized designs show a significant increase in the spar thickness, especially for the front spar. This is expected, as placing mass ahead of the elastic axis has stabilizing aeroelastic benefits. Additionally, increasing the spar thicknesses is the most mass-efficient way for the optimizer to increase the torsional stiffness of the wingbox, which mitigates flutter. The upper and lower skins also show a significant increase in mass compared with the baseline, except for the  $\alpha = 0^\circ$  case (the linear flutter analysis), where there is only a marginal increase. These sizing differences are attributed to the fact that the critical flutter modes for the non-zero angle of attack cases involve a different mechanism compared with the  $\alpha = 0^\circ$  case (discussed below), involving a geometrically nonlinear coupling of in-plane bending and torsion resulting from static

**Table 3 Optimization results (empty circle = inactive constraint, filled circle = active constraint).**

|                                      | Baseline | Flutter constraint angle of attack |               |                |
|--------------------------------------|----------|------------------------------------|---------------|----------------|
|                                      |          | 0°                                 | 3°            | 6°             |
| Wingbox mass [kg]                    | 68.5     | 76.1 (+11.1%)                      | 94.6 (+38.1%) | 104.6 (+52.7%) |
| KS <sub>flutter</sub>                |          | ●                                  | ●             | ●              |
| KS <sub>stress</sub> for ribs        | ○        | ○                                  | ○             | ○              |
| KS <sub>stress</sub> for spars       | ○        | ○                                  | ○             | ○              |
| KS <sub>stress</sub> for upper skins | ●        | ●                                  | ●             | ●              |
| KS <sub>stress</sub> for lower skins | ●        | ●                                  | ○             | ○              |

aeroelastic deflections [4, 24]. At non-zero angle of attack, the optimizer also uses the skin thickness to influence the stiffness associated with in-plane bending motions to delay flutter. At zero angle of attack, the optimizer delays flutter primarily by thickening the front spar. While the optimized design at  $\alpha = 6^\circ$  has the largest increase in skin thickness, the spars show a smaller increase compared to the optimized design at  $\alpha = 3^\circ$ .

The optimized structural sizing is reflected in the static aeroelastic response. Figure 6 shows the wing displacements normalized by the semispan and twist distribution along the span for all optimal designs at the maximum velocity considered in the flutter analyses, 180 m/s. The baseline out-of-plane bending tip displacements range from 0–50% of the semispan, compared to 0–29% across all optimized designs. Wing shortening effects are attenuated compared to the baseline design, demonstrating overall stiffer designs. Twist angles are also smaller in the optimized designs than the baseline: the optimized twist distribution along the span is closer to linear, while the baseline twist angles flatten closer to the tip due to geometrically nonlinear effects. Overall, the smaller static aeroelastic deflections in the optimized designs can be directly attributed to the increased spar thickness, resulting in a stiffer structure.

Figure 7 and Table 5 show the structural vibration modes of the wing in its undeformed configuration, where OOP, IP, and T refer to out-of-plane bending, in-plane bending, and torsion modes respectively. The offset location of the concentrated masses couples OOP bending and torsion in all designs, causing no pure torsional modes but several coupled bending-torsion modes. While the mode shapes are similar across all designs, the frequency values and frequency separation increase with the angle of attack considered in the flutter analysis because of the added structural thickness to satisfy the flutter constraint.

The flutter constraint is active for all optimized designs, as highlighted in the individual damping plots of Fig. 8. While the flutter analysis considers the complete set of aeroelastic modes, only the first four modes are visualized to highlight the critical modes. Figure 9 compares the optimized and baseline designs across all cases. Regardless of the angle of attack, the baseline design is flutter critical. In contrast, the previously unstable modes are pushed below the 0.12 rad/s damping threshold for all optimized designs at the velocity points used in the optimization.

The critical mode and flutter characteristics vary with the angle of attack and static deflection. For the undeformed case,  $\alpha = 0^\circ$ , the two fluttering modes for the baseline design are modes 3 and 4, which involve coupled out-of-plane bending and torsion. By increasing the thickness of the front spar, the optimizer slightly increases the frequencies of these modes but also, more importantly, alters the bend-twist coupling of the modes such that they have weaker damping characteristics. Mode 2, an in-plane bending mode, is unaffected by the optimization because it does not interact with aerodynamics for this undeformed case.

With non-zero angle of attack, i.e., including static aeroelastic deflections, the mode that originates from the in-plane structural mode 2, is the critical mode for the baseline design and remains active at both the  $\alpha = 3^\circ$  and  $\alpha = 6^\circ$  optimal designs. As mentioned above, this behavior is driven by the coupling of in-plane bending and torsion motions in the presence of static aeroelastic deflections and the optimizer attenuates this mode by increasing the thickness of both spars and skins of the wingbox.

## VI. Concluding Remarks

This paper presented a framework for high-fidelity, gradient-based wing structural optimization subject to a geometrically nonlinear flutter constraint. The framework evaluates the objective function (mass) and the stress and

**Table 4 Breakdown of the optimized mass [kg] and change relative to the baseline design.**

|            | Baseline  | Flutter constraint angle of attack |              |           |              |           |              |
|------------|-----------|------------------------------------|--------------|-----------|--------------|-----------|--------------|
|            |           | 0°                                 |              | 3°        |              | 6°        |              |
| Group      | Mass [kg] | Mass [kg]                          | $\Delta$ [%] | Mass [kg] | $\Delta$ [%] | Mass [kg] | $\Delta$ [%] |
| Ribs       | 4.8       | 6.3                                | 30.2         | 4.8       | 0.0          | 4.8       | 0.0          |
| Front spar | 3.4       | 5.5                                | 61.4         | 9.4       | 173.3        | 9.0       | 161.8        |
| Rear spar  | 2.8       | 3.1                                | 11.9         | 7.7       | 176.0        | 7.3       | 161.5        |
| Upper skin | 29.4      | 29.8                               | 1.2          | 35.9      | 21.9         | 40.9      | 39.1         |
| Lower skin | 28.1      | 30.4                               | 8.5          | 36.9      | 31.5         | 42.6      | 52.0         |

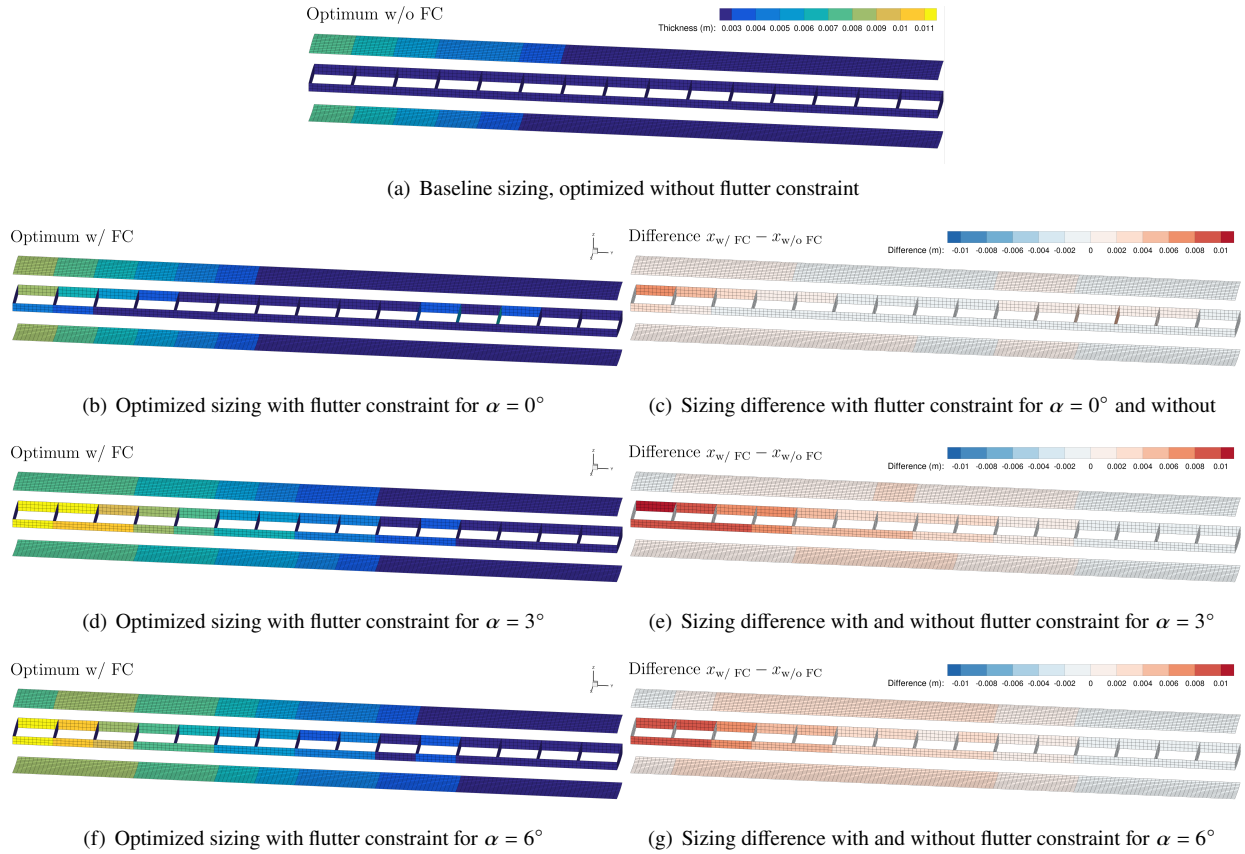


**Fig. 5 Comparison of the baseline and optimized structural sizing.**

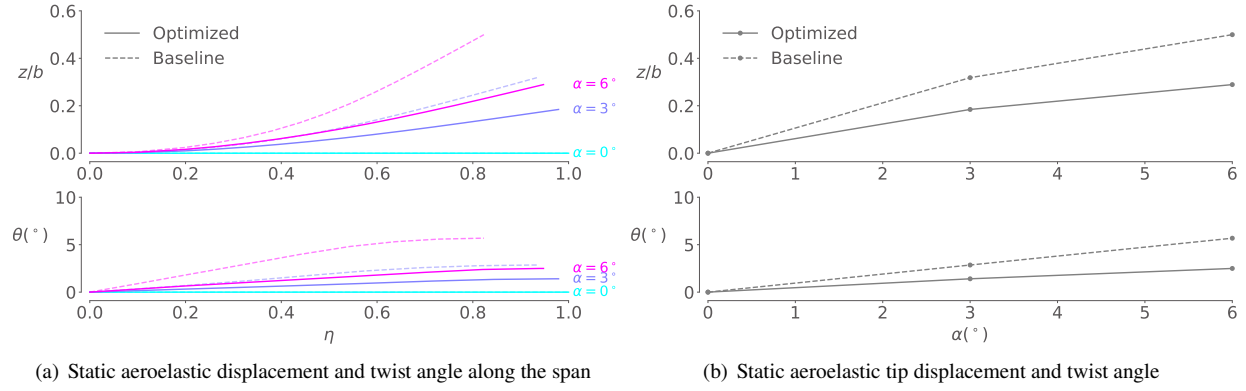


**Fig. 6** Static aeroelastic response of the baseline and optimized designs at  $V = 180$  m/s.

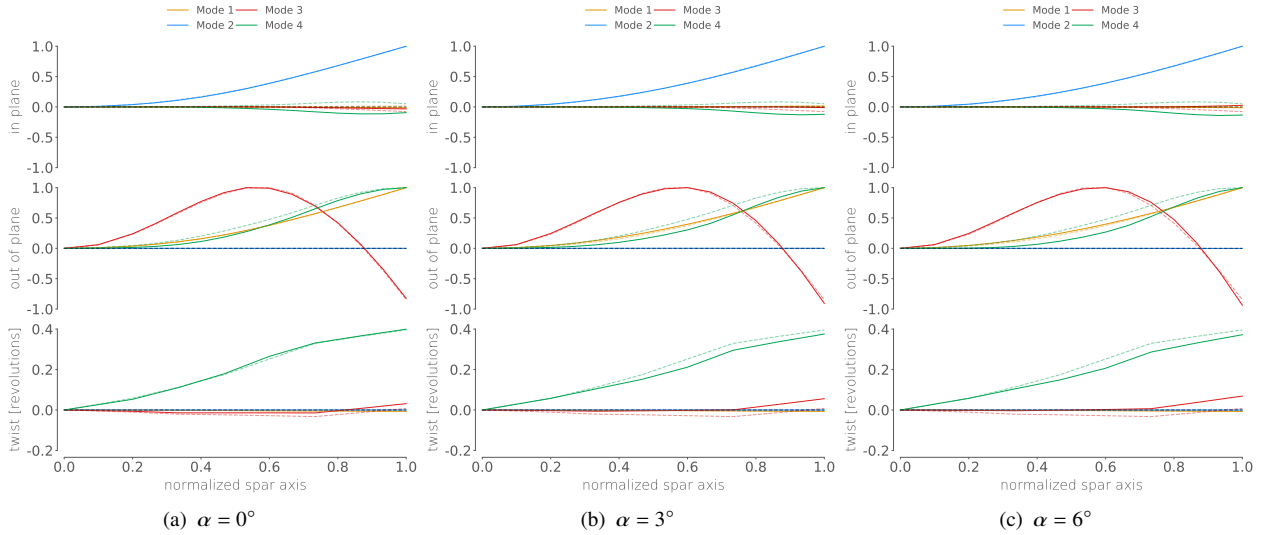


**Fig. 7** Mode shapes of the baseline (dash) and optimized (solid) designs.

**Table 5** Structural frequencies of the baseline and optimized designs.

| Mode | f [Hz] | Type    | Flutter constraint angle of attack |              |        |              |        |              |
|------|--------|---------|------------------------------------|--------------|--------|--------------|--------|--------------|
|      |        |         | 0°                                 |              | 3°     |              | 6°     |              |
|      |        |         | f [Hz]                             | $\Delta$ [%] | f [Hz] | $\Delta$ [%] | f [Hz] | $\Delta$ [%] |
| 1    | 3.44   | OOP1    | 3.47                               | 0.9          | 4.01   | 16.6         | 4.26   | 23.8         |
| 2    | 10.24  | IP1     | 10.60                              | 3.5          | 13.47  | 31.5         | 13.86  | 35.4         |
| 3    | 17.07  | IP2+T2  | 17.65                              | 3.4          | 17.63  | 3.3          | 18.13  | 6.2          |
| 4    | 28.37  | OOP1+T1 | 28.69                              | 1.1          | 34.32  | 21.0         | 36.11  | 27.3         |

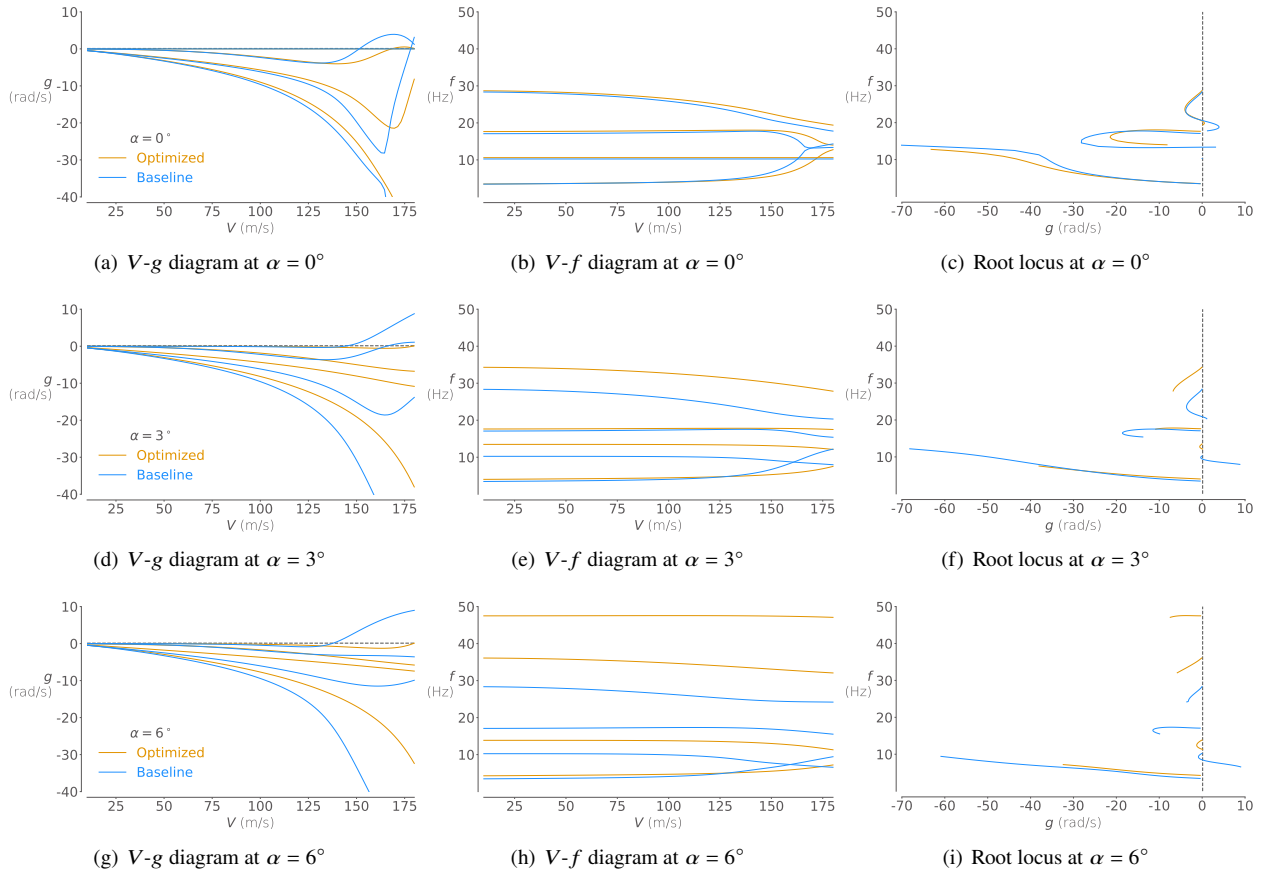


**Fig. 8 Flutter analysis of baseline and optimized designs for each angle of attack.**

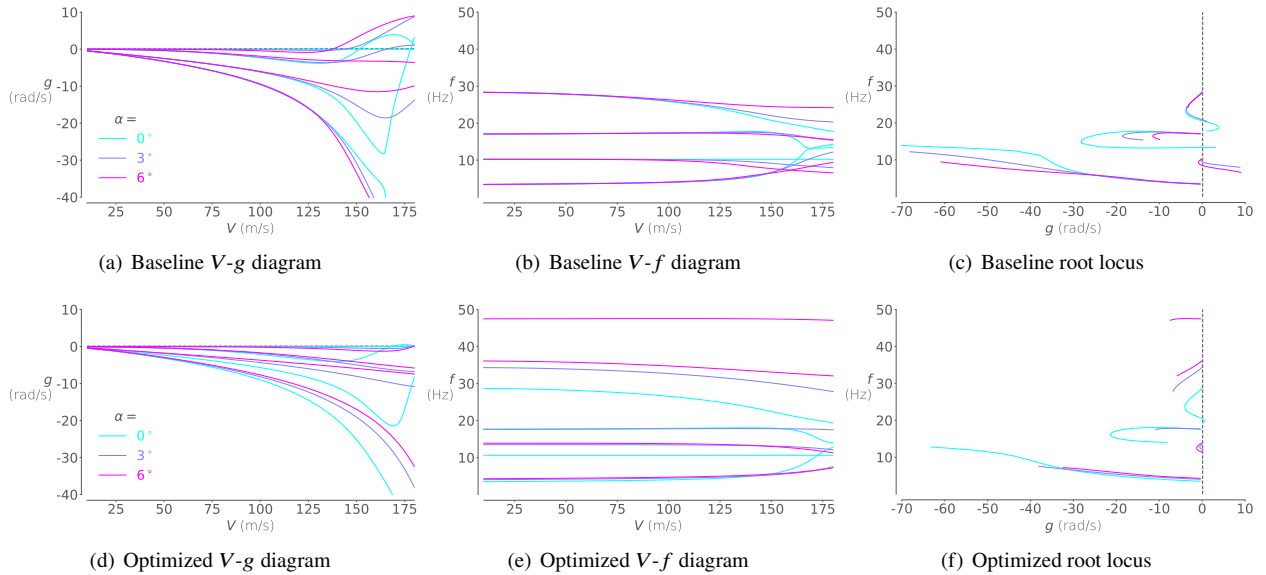


**Fig. 9 Flutter analysis of all baseline and optimized designs.**

adjacency constraints in a high-fidelity, built-up FEM to capture the realistic structural details. The built-up FEM at each optimization step is reduced to a low-order beam representation to make geometrically nonlinear flutter analysis tractable for optimization. The geometrically nonlinear flutter analysis considers the wing deformed shape at each flight condition and aggregates the associated damping values into a scalar flutter constraint.

The methodology was implemented into a computational environment that couples the built-up FEM solver TACS with the UM/NAST nonlinear aeroelastic solver using the EF2S framework to compute the equivalent beam representation of the built-up FEM at each optimization step. The total derivatives of the geometrically nonlinear flutter constraint evaluated using UM/NAST with respect to the TACS built-up FEM structural sizing variables were computed using the adjoint method. The methodology was demonstrated by minimizing the mass of a high-aspect-ratio wingbox subject to the geometrically nonlinear flutter constraint along with stress and adjacency constraints. The geometrically nonlinear flutter constraint added a mass penalty more than five times the one from a linear flutter constraint for the maximum angle of attack considered in the study. Using geometrically nonlinear analysis also revealed a different critical flutter mode, leading to significantly different thickness distributions in the optimized wingbox designs.

This work is a step toward considering geometrically nonlinear effects and dynamic aeroelasticity early in the aircraft design cycle to prevent flutter. Future work will investigate the impact of the structural model reduction and different geometrically nonlinear effects on the optimal design and include aerodynamic design variables.

### **Acknowledgments**

The material of this paper is based upon work supported by Airbus in the frame of the Airbus-Michigan Center for Aero-Servo-Elasticity of Very Flexible Aircraft. The authors thank Dr. Patrick Teufel (Airbus) for his review of the paper and for the technical discussions throughout this work.

## References

- [1] Afonso, F., Vale, J., Oliveira, É., Lau, F., and Suleman, A., “A Review on Non-Linear Aeroelasticity of High Aspect-Ratio Wings,” *Progress in Aerospace Sciences*, Vol. 89, No. Supplement C, 2017, pp. 40–57. doi:10.1016/j.paerosci.2016.12.004.
- [2] Cesnik, C. E. S., Palacios, R., and Reichenbach, E. Y., “Reexamined Structural Design Procedures for Very Flexible Aircraft,” *Journal of Aircraft*, Vol. 51, No. 5, 2014, pp. 1580–1591. doi:10.2514/1.C032464.
- [3] Patil, M. J., Hodges, D. H., and Cesnik, C. E. S., “Limit-Cycle Oscillations in High-Aspect-Ratio Wings,” *Journal of Fluids and Structures*, Vol. 15, No. 1, 2001, pp. 107–132. doi:10.1006/jfls.2000.0329.
- [4] Patil, M. J., Hodges, D. H., and Cesnik, C. E. S., “Nonlinear Aeroelasticity and Flight Dynamics of High-Altitude Long-Endurance Aircraft,” *Journal of Aircraft*, Vol. 38, No. 1, 2001, pp. 88–94. doi:10.2514/2.2738.
- [5] Patil, M. J., and Hodges, D. H., “Flight Dynamics of Highly Flexible Flying Wings,” *Journal of Aircraft*, Vol. 43, No. 6, 2006, pp. 1790–1799. doi:10.2514/1.17640.
- [6] Su, W., and Cesnik, C. E. S., “Nonlinear Aeroelasticity of a Very Flexible Blended-Wing-Body Aircraft,” *Journal of Aircraft*, Vol. 47, No. 5, 2010, pp. 1539–1553. doi:10.2514/1.47317.
- [7] Su, W., and Cesnik, C. E. S., “Dynamic Response of Highly Flexible Flying Wings,” *AIAA Journal*, Vol. 49, No. 2, 2011, pp. 324–339. doi:10.2514/1.53412.
- [8] Jonsson, E., Riso, C., Lupp, C. A., Cesnik, C. E. S., Martins, J. R. R. A., and Epureanu, B. I., “Flutter and Post-Flutter Constraints in Aircraft Design Optimization,” *Progress in Aerospace Sciences*, Vol. 109, 2019, pp. 1–28. doi:10.1016/j.paerosci.2019.04.001.
- [9] Variyar, A., Economou, T. D., and Alonso, J. J., “Design and Optimization of Unconventional Aircraft Configurations with Aeroelastic Constraints,” *2017 AIAA SciTech Forum*, Grapevine, TX, 2017, pp. 1–13. doi:10.2514/6.2017-0463, aIAA-2017-0463.
- [10] Xie, C., Meng, Y., Wang, F., and Wan, Z., “Aeroelastic Optimization Design for High-Aspect-Ratio Wings with Large Deformation,” *Shock and Vibration*, 2017, pp. 1–16. doi:10.1155/2017/2564314.
- [11] Lupp, C. A., and Cesnik, C. E. S., “A Gradient-Based Flutter Constraint Including Geometrically Nonlinear Deformations,” *2019 AIAA SciTech Forum*, San Diego, CA, 2019, pp. 1–22. doi:10.2514/6.2019-1212.
- [12] Jonsson, E., Mader, C. A., Kennedy, G. J., and Martins, J. R. R. A., “Computational Modeling of Flutter Constraint for High-Fidelity Aerostructural Optimization,” *2019 AIAA SciTech Forum*, San Diego, CA, 2019, pp. 1–27. doi:10.2514/6.2019-2354, aIAA-2019-2354.
- [13] Su, W., and Cesnik, C. E. S., “Strain-Based Geometrically Nonlinear Beam Formulation for Modeling Very Flexible Aircraft,” *International Journal of Solids and Structures*, Vol. 48, No. 16–17, 2011, pp. 2349–2360. doi:10.1016/j.ijsolstr.2011.04.012.
- [14] Riso, C., Sanghi, D., Cesnik, C. E. S., Vetrano, F., and Teufel, P., “Parametric Nonlinear Aeroelastic Analysis of a High-Aspect-Ratio-Wing Civil Transport Aircraft,” *2020 AIAA SciTech Forum*, Orlando, FL, 2020, pp. 1–23. doi:10.2514/6.2020-1191, AIAA-2020-1191.
- [15] Riso, C., and Cesnik, C. E. S., “Correlations between UM/NAST Nonlinear Aeroelastic Simulations and the Pre-Pazy Wing Experiment,” *2021 AIAA SciTech Forum*, Virtual Event, 2021, pp. 1–24. doi:10.2514/6.2021-1712, AIAA-2021-1712.
- [16] Peters, D. A., Hsieh, M. C. A., and Torrero, A., “A State-Space Airloads Theory for Flexible Airfoils,” *Journal of the American Helicopter Society*, Vol. 52, No. 4, 2007, pp. 329–342. doi:10.4050/JAHS.52.329.
- [17] Kreisselmeier, G., and Steinhauser, R., “Systematic Control Design by Optimizing a Vector Performance Index,” *Computer Aided Design of Control Systems*, Pergamon, 1980, pp. 113–117. doi:10.1016/B978-0-08-024488-4.50022-X.
- [18] Wrenn, G. A., “An Indirect Method for Numerical Optimization Using the Kreisselmeier–Steinhauser Function,” Tech. rep. cr-4220, NASA Langley Research Center, Hampton, VA, 1989.
- [19] Poon, N. M. K., and Martins, J. R. R. A., “An Adaptive Approach to Constraint Aggregation using Adjoint Sensitivity Analysis,” *Structural and Multidisciplinary Optimization*, Vol. 34, 2007, pp. 61–73. doi:10.1007/s00158-006-0061-7.
- [20] Kennedy, G. J., and Martins, J. R. R. A., “A Parallel Aerostructural Optimization Framework for Aircraft Design Studies,” *Structural and Multidisciplinary Optimization*, Vol. 50, No. 6, 2014, pp. 1079–1101. doi:10.1007/s00158-014-1108-9.



- [21] Gill, P. E., Murray, W., and Saunders, M. A., “SNOPT: An SQP algorithm for large-scale constrained optimization,” *SIAM Journal of Optimization*, Vol. 12, No. 4, 2002, pp. 979–1006. doi:10.1137/S1052623499350013.
- [22] Wu, N., Kenway, G., Mader, C. A., Jasa, J., and Martins, J. R. R. A., “pyOptSparse: A Python framework for large-scale constrained nonlinear optimization of sparse systems,” *Journal of Open Source Software*, Vol. 5, No. 54, 2020, p. 2564. doi:10.21105/joss.02564.
- [23] Perez, R. E., Jansen, P. W., and Martins, J. R. R. A., “pyOpt: A Python-Based Object-Oriented Framework for Nonlinear Constrained Optimization,” *Structural and Multidisciplinary Optimization*, Vol. 45, No. 1, 2012, pp. 101–118. doi:10.1007/s00158-011-0666-3.
- [24] Patil, M. J., and Hodges, D. H., “On the importance of aerodynamic and structural geometrical nonlinearities in aeroelastic behavior of high-aspect-ratio wings,” *Journal of Fluids and Structures*, Vol. 19, No. 7, 2004, pp. 905–915. doi:10.1016/j.jfluidstructs.2004.04.012.